

Electrolyte-gated transistors for synaptic electronics, neuromorphic computing, and adaptable biointerfacing

Citation for published version (APA):

Ling, H., Koutsouras, D. A., Kazemzadeh, S., van de Burgt, Y. B., Yan, F., & Gkoupidenis, P. (2020). Electrolyte-gated transistors for synaptic electronics, neuromorphic computing, and adaptable biointerfacing. *Applied Physics Reviews*, 7(1), Article 011307. <https://doi.org/10.1063/1.5122249>

Document license:

TAVERNE

DOI:

[10.1063/1.5122249](https://doi.org/10.1063/1.5122249)

Document status and date:

Published: 01/03/2020

Document Version:

Publisher's PDF, also known as Version of Record (includes final page, issue and volume numbers)

Please check the document version of this publication:

- A submitted manuscript is the version of the article upon submission and before peer-review. There can be important differences between the submitted version and the official published version of record. People interested in the research are advised to contact the author for the final version of the publication, or visit the DOI to the publisher's website.
- The final author version and the galley proof are versions of the publication after peer review.
- The final published version features the final layout of the paper including the volume, issue and page numbers.

[Link to publication](#)

General rights

Copyright and moral rights for the publications made accessible in the public portal are retained by the authors and/or other copyright owners and it is a condition of accessing publications that users recognise and abide by the legal requirements associated with these rights.

- Users may download and print one copy of any publication from the public portal for the purpose of private study or research.
- You may not further distribute the material or use it for any profit-making activity or commercial gain
- You may freely distribute the URL identifying the publication in the public portal.

If the publication is distributed under the terms of Article 25fa of the Dutch Copyright Act, indicated by the "Taverne" license above, please follow below link for the End User Agreement:

www.tue.nl/taverne

Take down policy

If you believe that this document breaches copyright please contact us at:




openaccess@tue.nl

providing details and we will investigate your claim.

Electrolyte-gated transistors for synaptic electronics, neuromorphic computing, and adaptable biointerfacing

Cite as: Appl. Phys. Rev. **7**, 011307 (2020); <https://doi.org/10.1063/1.5122249>

Submitted: 30 July 2019 . Accepted: 05 December 2019 . Published Online: 16 January 2020

Haifeng Ling , Dimitrios A. Koutsouras, Setareh Kazemzadeh , Yoeri van de Burgt , Feng Yan ,
and Paschalis Gkoupidenis 

COLLECTIONS

Paper published as part of the special topic on [Brain Inspired Electronics](#)

Note: This paper is part of the special collection on Brain Inspired Electronics.

 This paper was selected as an Editor's Pick



View Online



Export Citation



CrossMark

ARTICLES YOU MAY BE INTERESTED IN

[Brain-inspired computing with memristors: Challenges in devices, circuits, and systems](#)

Applied Physics Reviews **7**, 011308 (2020); <https://doi.org/10.1063/1.5124027>

[The building blocks of a brain-inspired computer](#)

Applied Physics Reviews **7**, 011305 (2020); <https://doi.org/10.1063/1.5129306>

[Ferroic tunnel junctions and their application in neuromorphic networks](#)

Applied Physics Reviews **7**, 011304 (2020); <https://doi.org/10.1063/1.5120565>



Applied Physics Reviews

Submit your original research today!

LEARN MORE >>>

Journal
Impact Factor
12.750

AIP
Publishing

Electrolyte-gated transistors for synaptic electronics, neuromorphic computing, and adaptable biointerfacing

Cite as: Appl. Phys. Rev. **7**, 011307 (2020); doi: [10.1063/1.5122249](https://doi.org/10.1063/1.5122249)

Submitted: 30 July 2019 · Accepted: 5 December 2019 ·

Published Online: 16 January 2020






View Online



Export Citation



CrossMark

Haifeng Ling,^{1,2,3}  Dimitrios A. Koutsouras,³ Setareh Kazemzadeh,⁴  Yoeri van de Burgt,⁴  Feng Yan,^{2,a)}  and Paschalis Gkoupidenis^{3,a)} 

AFFILIATIONS

¹Institute of Advanced Materials (IAM), Nanjing University of Posts & Telecommunications, Nanjing 210023, China

²Department of Applied Physics, Hong Kong Polytechnic University, Hong Kong, China

³Department of Molecular Electronics, Max Planck Institute for Polymer Research, Mainz 55128, Germany

⁴Microsystems, Institute for Complex Molecular Systems, Eindhoven University of Technology, Eindhoven 5612AJ, The Netherlands

Note: This paper is part of the special collection on Brain Inspired Electronics.

^{a)}Authors to whom correspondence should be addressed: apafyan@polyu.edu.hk and gkoupidenis@mpip-mainz.mpg.de

ABSTRACT

Functional emulation of biological synapses using electronic devices is regarded as the first step toward neuromorphic engineering and artificial neural networks (ANNs). Electrolyte-gated transistors (EGTs) are mixed ionic–electronic conductivity devices capable of efficient gate-channel capacitance coupling, biocompatibility, and flexible architectures. Electrolyte gating offers significant advantages for the realization of neuromorphic devices/architectures, including ultralow-voltage operation and the ability to form parallel-interconnected networks with minimal hardwired connectivity. In this review, the most recent developments in EGT-based electronics are introduced with their synaptic behaviors and detailed mechanisms, including short-/long-term plasticity, global regulation phenomena, lateral coupling between device terminals, and spatiotemporal correlated functions. Analog memory phenomena allow for the implementation of perceptron-based ANNs. Due to their mixed-conductivity phenomena, neuromorphic circuits based on EGTs allow for facile interfacing with biological environments. We also discuss the future challenges in implementing low power, high speed, and reliable neuromorphic computing for large-scale ANNs with these neuromorphic devices. The advancement of neuromorphic devices that rely on EGTs highlights the importance of this field for neuromorphic computing and for novel healthcare technologies in the form of adaptable or trainable biointerfacing.

Published under license by AIP Publishing. <https://doi.org/10.1063/1.5122249>

TABLE OF CONTENTS

I. INTRODUCTION	1
II. ION TRANSPORT IN NEUROMORPHICS	4
III. NEUROMORPHIC DEVICES AND FUNCTIONS	6
A. Synaptic plasticity and global phenomena	6
B. Biofriendly materials and mechanically flexible electrolytes	9
C. Spatially correlated functions	10
D. Perceptron-based artificial neural network	13
E. Neuromorphic sensing and biointerfacing	15
1. Synaptic coupling of living neurons	15
2. Artificial sensory systems	15
IV. SUMMARY AND PERSPECTIVES	18

I. INTRODUCTION

Present digital computation relies on the von Neumann architecture as implemented with complementary metal-oxide-semiconductor (CMOS) technology. Due to current limitations in semiconductor manufacturing technology, modern computer systems typically employ hierarchical storage and memory-processor discrete approaches to achieve an optimal balance between computational performance and computational cost. With this approach, parallel processing is challenging, an issue commonly referred to as the von Neumann bottleneck.¹ A neural system, such as the mammalian brain, is an efficient information-processing system, which contains about 10^{11} neurons to form 10^{15} synaptic connections.² Through this specific structure, our brain is massively parallel and offers distributed computation, which

combines processing and memory together with a very low power consumption of ~ 20 W. Neuromorphic devices, which aim to emulate functions of biological neurons and synapses, may provide new building blocks for the post-Moore law era. In this scenario, neuromorphic computing is regarded as a promising computing paradigm for future artificial intelligence (AI), big data analysis, Internet of Things (IoT), etc.^{3,4} Since the European Union and the United States took the lead in launching their Human Brain Project (HBP) and Brain Research through Advancing Innovative Neurotechnologies (BRAIN) in 2013, more and more countries and research institutes have been accelerating investments in brain-inspired technology worldwide. Another

purpose of the brain-related research projects is to enable a better understanding of the principles of information processing in the brain, with an ultimate goal to understand malfunctions and find new ways to cure brain diseases.

Neurons and synapses in the brain are the smallest unit of learning and memory. As shown in Fig. 1(a), a synapse is the nanogap (~ 3.5 nm) that connects two neurons, which can receive and process massive presynaptic inputs to determine the postsynaptic outputs.⁵ The synaptic weight (W), i.e., the connection strength between neurons, depends on the concentrations of ionic species (e.g., Ca^{2+} , Na^+ , and K^+) upon presynaptic action potentials (APs), which modulate

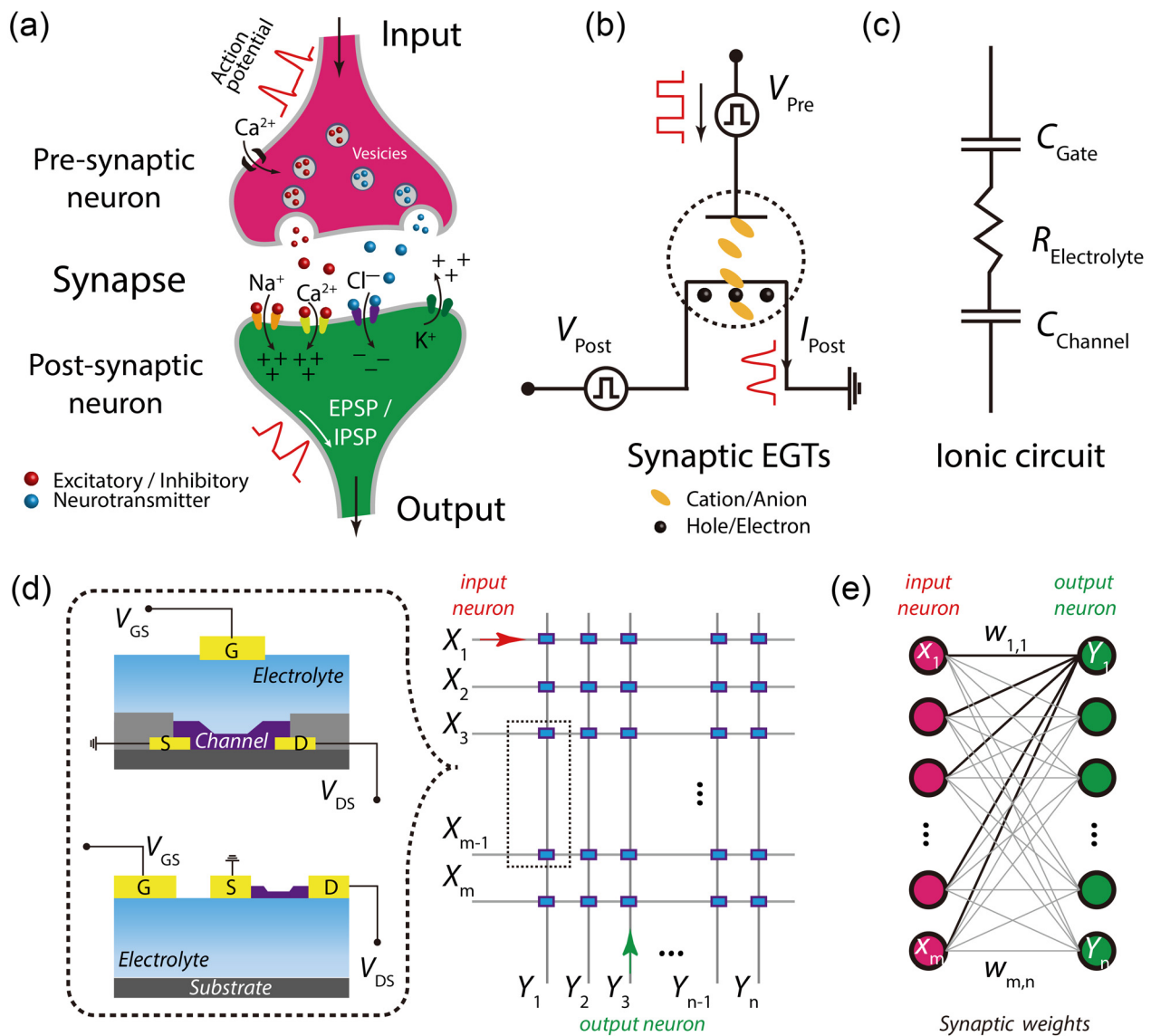


FIG. 1. Schematic illustration of (a) a biological synapse and (b) the EGT-based artificial synapse. (c) Ionic circuits used to model EGTs. (d) The circuits for a voltage-controlled crossbar array. Synaptic EGTs that encode the synaptic weights are present at each cross point. Diagrams indicated in the dashed frame are two typical device structures of EGTs. (e) Schematics of a single-layer perceptron (SLP)-based network. Artificial neural networks connect an input layer to an output layer using hidden layers (synaptic weights, W). The synaptic weight ($W_{m,n}$) between each input (X_m) node and output (Y_n) node can be modulated to train the network to perform the desired operation.

the release of neurotransmitters. The synaptic weight permits the coupling between neurons, conveying electrical or chemical signals and influencing the spiking behavior of neighboring neurons, giving thus rise to the neuronal development. Changes in synaptic strength are known as synaptic plasticity. In neurology, synaptic plasticity is activity dependent at either or both sides of the synapse.⁶ Generally, synaptic plasticity can be classified into short-term plasticity (STP) and long-term plasticity (LTP), respectively. STP corresponds to the transient modification of synaptic strength after stimulation, which lasts for tens of milliseconds to a few minutes, while LTP is a persistent modification of synaptic strength, which can last from hours to years. In biological systems, STP is required for short-term memory (STM) and allows synapses to perform critical computational functions in neural circuits such as transmission, encoding, and filtering of neuronal signals.⁷ However, LTP is obviously needed for storing the processed information, i.e., the long-term memory (LTM), and is thought to underpin learning and memory.⁸ STP can be converted to LTP after sufficient training or persistent neuronal activities. A putative neuronal mechanism of learning and memory is Hebbian synaptic plasticity, i.e., the synaptic strength between the pre- and postsynaptic neurons depends on the time-correlation of their activity.^{9,10} Two classic paradigms for the induction of Hebbian plasticity is spike-timing-dependent plasticity (STDP) and spike-rate-dependent plasticity (SRDP).¹¹ STDP is the refinement of the Hebbian rule, where the synaptic modification relies on the relative timing of activity between the pre- and postsynaptic neurons.¹² STDP is considered to be the main learning and memory mechanism of the brain and also forms the basis for autonomous, unsupervised learning in neuromorphic computing.¹³ SRDP is another widely observed learning rule, which reflects the influence of the activity frequency of presynaptic inputs on synaptic modification.¹⁴

Hardware implementation of synaptic functionalities using microelectronic devices is regarded as the footstone for neuromorphic engineering. Multiple and nonvolatile conductance levels of electronic devices are needed to mimic the basic functions of synaptic plasticity. Presently, there are two possible ways of synapse realization: the traditional silicon hardware and the emerging memory devices. The main advantage of the former is the maturity of silicon and its full integration with the standard CMOS technology. Mead *et al.* coined the term “neuromorphic” in the 1980s and proposed the concept of a single transistor learning synapse in 1995.^{15,16} The silicon approach relies on charge-based mechanisms as in conventional flash memory and random access memory (RAM), such as static and dynamic RAM (SRAM and DRAM). Several MOS transistors are usually needed to build a silicon neuron.¹⁷ With the development of semiconductor manufacturing technologies over the past two decades, nonbiomimetic CMOS chips have been the advanced electronic implementation of neuron circuitry. Brain-like circuits are now commercially available, by integrating billions of transistors on a square centimeter.^{18–20} However, the need for high speed and design complexity for CMOS architectures complicate the path to achieve the interconnectivity, information density, and energy efficiency of the brain. Unlike the “0” and “1”-based digital transistors that make up modern computer chips, alternative analog devices with nonlinear transmission characteristics and slow ion motions are closer to the biophysical properties of neurons and synapses. In addition, analog computing without using analog-to-digital or digital-to-analog (ADC/DAC) conversion is not

only energy efficient but has great potential in a mixed-signal neural network.²¹ Although the appropriate candidates for artificial synapses and neurons is still under debate, tunable memory devices including two-terminal memristors and three-terminal neuromorphic transistors are promising.^{3,22} The operation principles of these devices are based on coupled ionic-electronic features.²³ The original definition for memristor (“memory resistor”) was predicted from symmetry arguments by Chua in 1971.²⁴ In 1976, Chua *et al.* generalized the memristor concept to a much broader class of nonlinear dynamical systems they called memristive systems.²⁵ In 2008, Strukov *et al.* correlated the resistive switching devices with memristors, in which memristance was experimentally observed in Pt/TiO_x/Pt memories.^{26,27} The resistance of the devices depends on the history of current that has flowed through it under an external bias voltage. Note that the roots of resistive switching phenomena date back to the 1960s,^{28,29} while resistive switching devices were proposed as a new generation of nonvolatile memories even before the experimental evidence of memristors.³⁰ The pinched hysteresis loop has been identified as the fingerprint of memristive systems,^{31,32} thereby unifying a broad class of two-terminal nonvolatile memories as memristors. These devices include resistive switching RAM (RRAM),^{33–35} magnetic RAM (MRAM),³⁶ and phase-change memory (PCM).³⁷ Over the last decade, memristors were intended for applications in data storage, logic circuits, and neuromorphic computing. In particular, for neuromorphic applications, abrupt switching that is present in conventional binary memristors (i.e., digital-type memories) is unfavorable, and analog memory phenomena are desirable for the training of neural networks with high accuracy/speed.^{38,39} The gradual switching can be engineered by redox reactions (e.g., electrochemical metallization, and valence change),⁴⁰ the current-induced Joule heating effect,⁴¹ the spin-transfer torque effect,⁴² and even ferroelectric polarization.⁴³ For the redox-based resistive switching memristors that are coupled by ionic and electronic transport dynamics, aspects such as electrolyte materials,^{44,45} electrode activity,⁴⁶ filament nucleation,^{47,48} and ambient⁴⁹ have been extensively studied to achieve controllable switching characteristics. Nowadays, memristors have attracted great interest for single synaptic units with high scalability (<2 nm), 3D integration capability, and fast switching speed (~nanosecond).⁵⁰ Large area arrays of memristors could be easily integrated in a crossbar architecture to perform vector-matrix multiplication directly utilizing Ohm’s law and Kirchhoff’s law.²¹ Complex computational tasks and artificial neural networks (ANN) have been implemented with such post-CMOS device arrays.^{51–53}

On the other hand, neuromorphic transistors could provide an alternative platform for synaptic electronics because of their structural nature, with physically separated input and output terminals.^{54–56} Hysteresis in the transfer curves of transistors with gradually changed conductance presents a history-dependent memory behavior. Hence, the synaptic weight (i.e., channel conductance, G) can be precisely controlled in a tightly coupled fashion between the control terminal (gate electrode) and the transduction terminals (source–drain electrodes). Meanwhile, the training or “write” operation is on the gate that is spatially separated from the signal transmission or the “read” process on the channel. This endows synaptic circuits with concurrent actualization of inference and learning, hence facilitating the implementation of more complex neuromorphic functions.⁵⁷ Besides, the write current (i.e., gate current) could be much lower than the read current (drain

current) so that this three-terminal configuration results in improved state retention and energy efficiency.⁵⁸ From the mechanism perspective, neuromorphic transistors are desirable for the decoupling of STP and LTP through the use of different functional regions and physical mechanisms,^{59–61} thus being a naturally suitable medium in which STP and LTP can be induced concomitantly and expressed independently.⁶² From other performance and functionality viewpoints, neuromorphic transistors offer advantages of multimodal control (e.g., electrical, optical, mechanical stimuli, and physicochemical responses such as gas and ion/molecular sensing^{63–66}), thereby allowing the implementation of artificial synapses that mimic biological sensory (afferent) and motor (efferent) neurons.^{67,68}

Among all kinds of neuromorphic transistors, electrolyte-gated transistors (EGTs), in which the semiconducting channel is in contact with a gate electrode via an electrolyte [Fig. 1(b)], have shown to be very promising for the implementation of artificial synapses. The electrolyte is an ionic conductor but an electronic insulator dielectric.⁶⁹ An electrolyte could be either in a liquid or a solid state, having ions (anions and cations) displaced in opposite charges at the electrolyte/electrode interfaces in response to an electric field. Typically, two major categories of EGTs have been employed for synaptic electronics depending on the permeability of the semiconductor channel to the ions of the electrolyte. Specifically, the impermeable one is the electrolyte-gated field-effect transistor (EG-FET) with the channel current modulated by the gate voltage via a capacitive field-effect mechanism at the channel/electrolyte interface. Due to the ultrathin “electrical double layers” (EDLs, ~ 1.0 nm) formed at the gate/electrolyte and electrolyte/semiconductor interfaces, EG-FET is often known as electrical double layer transistors (EDLTs). The other type is called an electrochemical transistor (ECT), which is based on electrochemical doping/dedoping processes upon the bulk injection of ionic species to the redox-active channel material. Previously, EGTs have been widely used in chemical and biological sensing, which was enabled by their high transconductance and compatibility with aqueous solutions and biological systems.^{70–72} The interest in EGTs dramatically increased in recent years after being associated with the concept of neuromorphic transistors. Compared to dielectric thickness-dependent field-effect transistors (FETs, nF/cm^2), EGTs employ a high parallel plate capacitance ($\sim 1\text{--}10\ \mu\text{F/cm}^2$) and/or volumetric capacitance ($\sim 370\ \text{F/cm}^3$ or $\sim 500\ \mu\text{F/cm}^2$ equivalent capacitance/unit area) to realize the high coupling efficiency of the gate to the channel.⁷³ This feature endows synaptic EGTs with the ability to alter conductance at ultralow voltages (\sim millivolt), leading to an attractive alternative in energy-efficient neuromorphic circuits.⁷⁴ Moreover, coupled and tunable ionic and electronic conductances make EGTs valuable for electronic synapses [Fig. 1(c)] since their operation mode approaches the biological counterparts when compared to other technologies. For these reasons, EGTs can be exploited for the realization of electronic prostheses to directly interface with living neurons that have signals of low amplitude.⁷⁵ Another benefit of the synaptic EGTs is their structural flexibility in constructing the synaptic networks. A shared electrolyte would be an interesting feature to provide a global control mechanism (one-input to multioutputs).⁷⁶ On the other hand, an electrolyte is particularly suitable for the lateral-gated transistor configuration [Fig. 1(d)], enabling multi-inputs to one-output.⁷⁷ In this regard and given the specific characteristics of EGTs (e.g., ion/electron interaction, high specific capacitance, physiological environmental compatibility, and

architectural flexibility), a unique opportunity arises to explore these devices as candidates for neuromorphic building blocks with new and unconventional form factors [Fig. 1(e)].^{22,68,78}

In this review, the recent advances in EGT-based synaptic electronics, from a single device to neural networks, are comprehensively summarized and discussed. A brief theoretical background of static and transient characteristics for EGTs is introduced in Sec. II. In Sec. III, recent developments of synaptic responses and artificial perception neurons are reviewed based on the electrolyte gating of metal oxides, organic materials, and 2D materials. Finally, challenges and perspectives for future research of synaptic electronics and neuromorphic systems based on electrolyte-gated transistors are discussed in Sec. IV.

II. ION TRANSPORT IN NEUROMORPHICS

In biological synapses, signals are carried via the exchange of various ionic or molecular species. The action potential opens the voltage-gated calcium channels of the presynaptic membrane, leading to the secretion of neurotransmitter vesicles at the synaptic cleft.⁷⁹ Neurotransmitters are defused through the synaptic cleft and bind to receptors of the postsynaptic membrane to activate ion channels. The influx of ions at the postsynaptic membrane alters the polarization state of the neuron, and action potentials are fired if a depolarization threshold is exceeded.⁸⁰ Therefore, neuromorphic devices that involve signals of ionic or molecular nature are desirable due to their biological relevance during device operation.

There are different approaches to implement coupled ionic and electronic conductivities in artificial synapses to emulate the biological synaptic functionality. The concept of using electrolytes in contact with semiconducting materials is not a new one. It dates back in the ‘50s when researchers at Bell labs were experimenting with germanium electrodes interfacing the aqueous solution of potassium hydroxide, potassium chloride, and hydrochloric acid.⁸¹ These experiments showed that electrolytes can be efficiently used to modulate the semiconductor surface potential, validating the idea that they can also be employed for transistor gating. The motivation behind that was to take advantage of the large capacitance electrolytes can deliver, which allows for extremely low operation voltages. In this part, as a case study, we mainly focus on organic electrolyte-gated transistors, and specifically, we are going to present their basic operation mechanism and provide the main equations that govern their steady state and transient response. To achieve this, we categorize electrolyte-gated transistors in two major classes.⁸² The first one includes transistors the semiconducting film of which is impermeable to the electrolyte ions [Fig. 2(a)], while in the second class, these ions can penetrate the semiconductor, changing its redox state [Fig. 2(b)].

In the impermeable mode of operation, an applied gate voltage forces ions to migrate to and pile up at the gate/electrolyte and electrolyte/semiconductor interfaces. These ions screen charges at the gate and accumulate (or deplete) carriers in the semiconducting film. As a result, EDLs are formed at both interfaces, which can be considered as capacitors with a Debye screening length λ at the nanometric scale. In this case, the thickness of the dielectric is reduced to an interface level, resulting in a high parallel plate capacitance. The specific capacitance of these nanocapacitors can be estimated to $10\ \mu\text{F/cm}^2$, a value significantly larger than the typical $0.1\ \mu\text{F/cm}^2$ achieved by solid-state dielectric capacitors.^{82,83} It is also worth noticing that for these devices, the applied gate potential drops predominantly at the formed double layer

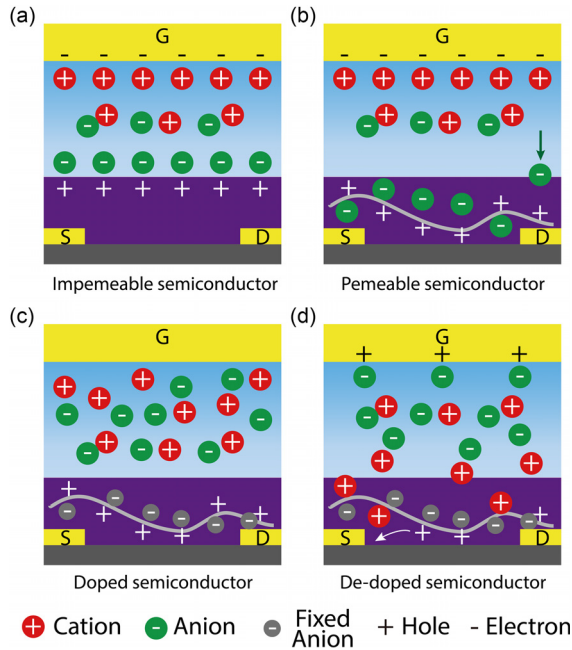


FIG. 2. Typical architecture of EGTs. Accumulation-mode operation of an EGT for (a) undoped ion-impermeable and (b) permeable semiconductors. Depletion-mode operation for conducting polymers (e.g., PEDOT:PSS) (c) without and (d) with positive gate voltage.

capacitors, while the voltage remains constant in the bulk of the (electrically neutral) electrolyte. The above fact implies that the operation of an impermeable EDL transistor can be considered an extreme case of a FET.

Therefore, for the steady state regime, the channel current is given by an equation similar to the one derived for FETs⁸⁴

$$I_{DS} = \frac{W}{L} \mu C' \left[(V_G - V_{Th}) V_D - \frac{V_D^2}{2} \right], \quad (1)$$

where W and L are the channel width and length, μ is the charge carrier mobility, C' is the capacitance of the dielectric per unit area, V_{Th} is the threshold voltage, V_D is the source drain bias, and V_G is the voltage applied at the gate electrode.

Regarding the transient analysis, the current can be expressed as the sum of the initial and the charging currents.⁸⁵ In this approach, the Ward-Dutton model was adopted in an electrolyte-gated FET in order for the terminal charges and capacitances to be calculated and consequently the charging currents to be obtained. Finally, the transient drain and source currents are given as follows:

$$i_D(t) = I_{D0}(t) + \frac{dQ_D(t)}{dt}, \quad (2)$$

$$i_S(t) = I_{S0}(t) - \frac{dQ_S(t)}{dt}, \quad (3)$$

where $I_{D0}(t)$ and $I_{S0}(t)$ are the initial currents and $Q_D(t)$ and $Q_S(t)$ the charges at the drain and source, respectively.

For the permeable mode, the electrolyte ions can penetrate the semiconductor film, thereby modulating its conductivity, a process called electrochemical reaction. The EDL at the gate/electrolyte

interface in this case may or may not be formed depending on the gate material employed (polarizable or nonpolarizable gate electrodes). Transistors that work in this configuration are called electrochemical transistors (ECTs), and the redox is a reversible process taking advantage of the entire volume of the conducting film and delivering large volumetric capacitance values.⁸⁶ As a result, small changes in gate biases result in large modulations in drain current, which is the reason for ECTs to operate as efficient switches and powerful amplifiers. Organic electrochemical transistors (OECTs) often employ a conducting polymer that is electrochemically active and ion permeable. With the right choice of the channel material, the device can operate either in the accumulation or the depletion mode [Fig. 2(c)].⁸⁷ Specifically, for the latter mode, [poly(3,4-ethylenedioxythiophene) doped with poly(styrene sulfonate) (PEDOT:PSS)], an archetypical conductive p-type polymer blend consisting of hole conductive PEDOT oligomers polymerizing in the ion conductive PSS template, has been widely exploited in biosensing and neuromorphic applications. PEDOT:PSS can undergo an oxidation/reduction reaction and switch between the conducting (oxidized) PEDOT⁺ and the insulating (neutral) PEDOT⁰ electrochemical states. The PSS chain is hydrophilic and ion permeable. Applying a positive bias at the gate leads to the injection of cations into the polymer blend [Fig. 2(d)]. Therefore, the positive bias at the gate leads to the diffusion of cations into the PSS structure and the compensation of the sulfonic acid groups of PSS. At the same time, PEDOT charge carriers (polarons and bipolarons) hop between PEDOT regions through π - π stacking. This mechanism thus provides both ionic and electrical conductivities in the channel. The charge neutrality of the PEDOT:PSS layer implies a reduction in the number of holes in the polymer, which is similar to electrochemically dedoping. These excess holes are extracted at the drain electrode, and since the drain current is proportional to the quantity of mobile holes in the channel, it probes the doping state of the organic polymer.⁷³

The steady state current in a device like that is given by a formula that bares similarities to (1)

$$I_{DS} = \frac{W \cdot d}{L} \mu C^* \left[(V_{Th} - V_G) V_D - \frac{V_D^2}{2} \right], \quad (4)$$

where W , L , and d are the channel width, length, and thickness, respectively, μ is the charge carrier mobility, C^* is the capacitance per unit volume of the channel, V_{Th} is the threshold voltage, V_D is the source drain bias, and V_G is the voltage applied at the gate electrode. The figure of merit of the conducting polymer can be defined by the product of the charge-carrier mobility and volumetric capacitance ($\mu \cdot C^*$).⁸⁶ Equation (4) for ECTs is similar to Eq. (1) for EG-FETs, with the difference that the product of channel thickness (d) and volumetric capacitance ($d \cdot C^*$) replaces C' . This variation defines the difference between the two devices.

Finally, when it comes to the transient response, a quasistatic approximation ignores the spatial voltage and charge density variations and averages the ionic current and charge density. As a result, the transient drain current is simplified to⁸⁸

$$I(t, V_G) = I_{ss}(V_G) + \Delta I_{ss} \left(1 - f \frac{\tau_e}{\tau_i} \right) \exp\left(-\frac{t}{\tau_i}\right), \quad (5)$$

where $I_{ss}(V_G)$ is the steady-state source-drain current at a gate voltage V_G and ΔI_{ss} is the difference between the current for gate voltage V_G minus the current voltage for gate voltage $V_G = 0$ and f a proportionality

constant to account for the spatial nonuniformity of the dedoping process.

Various semiconducting materials have been actively examined in synaptic EGTs. Note that the ionic dynamics in EGTs are complicated, and ionic gating modes could be modulated by varying the stimulation conditions on the gate terminal, such as the width, frequency, and polarity of the gate pulses, which serve as the driving force of ion migrations toward the rigid or soft channel materials. The most common classes of channel materials consist of rigid metal-oxide semiconductors [indium-zinc-oxide (IZO),^{89,90} indium gallium zinc oxide (IGZO),^{91–93} and indium-strontium-zinc-oxide (ISZO)⁹⁴], binary metal-oxides [zinc oxide (ZnO)⁹⁵], perovskite oxides [tungsten oxide WO₃ (Ref. 61)], 2D materials [graphene,^{96–98} MoS₂,^{59,99,100} α -MoO₃,^{101,102} WSe₂,¹⁰³ etc.], 1D materials [carbon nanotubes (CNTs),^{104,105} InP nanowires,¹⁰⁶ and polymer nanowires^{107,108}], and soft organic semiconductors [PEDOT:PSS,^{58,109} poly(3-hexylthiophene) (P3HT),^{110,111} polyaniline (PANI),^{112,113} 2,7-dioctyl[1]benzothieno[3,2-b][1]benzothiophene (C8-BTBT),¹¹⁴ pentacene,¹¹⁵ etc.]. The large free volumes in the conjugated polymer (CP) bulk can also transport ions, leading to an extremely high transconductance dictated by the volumetric capacitance (C^*).⁸⁶ Amorphous oxide semiconductor-based synaptic EGTs have a combination advantages of high mobility, transparency, and inherent persistent photoconductivity (PPC) by optimizing the metallic composition ratios.⁹⁴ These inorganic semiconductors could be deposited either by solution-processing or magnetron sputtering with uniform properties in large scale production. They can act as both an electrode and a channel,¹¹⁶ like the way of conducting polymer PEDOT:PSS.¹¹⁷

III. NEUROMORPHIC DEVICES AND FUNCTIONS

The biologically inspired neuromorphic systems are expected to be capable of dealing with complex and intelligent tasks, where neuromorphic functionalities need to be implemented at the single device or circuit level. Below, the basic principles of neuromorphic devices and functions are presented.

A. Synaptic plasticity and global phenomena

Synaptic plasticity, i.e., the ability of synapses to modulate the coupling between the pre- and the postsynaptic neurons, leads to the dynamic development of the neuronal network. For synaptic plasticity, there are two forms of synaptic responses, namely, potentiation and depression, which are linked to the strengthening and weakening of synaptic transmission, respectively.¹¹⁸ For STP, short-term potentiation (STPo) and short-term depression (STD) in synapses act as high-/low-pass filtering that plays a significant role in the information processing of auditory and visual system.¹¹⁹ STP in the form of amplitude encoding is also believed to enhance the bandwidth of neurons whenever saturation in their rate code is reached.¹²⁰ For LTP, it is now clear that long-term potentiation (LTPo) and long-term depression (LTD) are used for multiple brain functions in addition to learning and memory, as it contributes to the neuronal development.^{121,122} Fundamental synaptic plasticity behaviors have been successfully mimicked in electrolyte-gated synaptic transistors, such as excitatory/inhibitory postsynaptic current (EPSC/IPSC), paired pulse facilitation/depression (PPF/PPD), and high/low-pass filtering effects, and spike-timing-dependent plasticity (STDP).

The electrostatic coupling effect has been widely used to mimic the STP functions in dense semiconductor-based EDLTs.¹²³ Chen *et al.* reported on a carbon nanotube (CNT) channel synapse with a hydrogen-doped poly(ethylene glycol) (PEG) electrolyte.^{105,124} When the presynaptic spike was low and short (5 V, 1 ms), the dynamic change of postsynaptic current (PSC, channel current) was induced by the hydrogen ion accumulation at the electrolyte/channel interface, which in turn modified the electron concentration in the CNT channel.⁸³ Such an interfacial EDL electrostatic modulation process was reversible when the gate voltage was removed, representing the temporal analog phenomenon in biological synapses. The CNT synaptic device showed dynamic signal processing and learning functions with an extremely low energy of ~ 7.5 pJ/spike. In contrast to the two-terminal memristive devices in which the energy consumption is mainly contributed by the write operation, the read energy of synaptic EGT is comparable or larger than the write energy because the gate leakage current is generally much lower than the channel current, and thus, the energy efficiency is read limited.^{101,125} The overall energy consumption scales with the channel area.⁷⁴ Channel materials with inherently low conductivity are more suitable to construct energy-efficient synaptic EGTs.⁵⁸

The STP functions based on the electrochemical doping concept were initially demonstrated by Gkoupidenis *et al.* in PEDOT:PSS based organic electrochemical transistors (OECTs) gated with an aqueous KCl electrolyte (0.1 M).¹⁰⁹ In this depletion-mode transistor, synaptic functions were reproduced by applying positive presynaptic voltage pulses (V_{Pre}) at the gate electrode (with amplitude V_p , width t_p , period T_p , and time interval between the pulses $\Delta t = T_p - t_p$). Cations (K^+) were injected from the electrolyte to the soft PEDOT:PSS blend, resulting in the compensation of the sulfonic acid groups of PSS and the charge neutrality of the PEDOT:PSS layer. This electrochemically dedoping lost mobile holes in PEDOT:PSS and thereby induced an inhibitory postsynaptic current (IPSC). After removing the pulse, the injected cations relax to the electrolyte, and the PEDOT:PSS layer was reversibly doped to its initial high-conductance state, showing a typical short-term depression behavior. The PPD behavior was mimicked by applying a pair of pulses at the gate electrode [Fig. 3(a)]. The depression percentage decreased with the increasing time interval Δt . High frequency presynaptic stimuli were heavily suppressed, enabling the depressive PEDOT:PSS OECT to serve as a low-pass filter that impedes supernumerary bursts of presynaptic pulses. Frequency-dependent high- or low-pass filtering could be realized in a single device depending on the patterns of presynaptic activity.^{126,127} For example, Ling *et al.* reported an identical spike-polarity method to mimic the concomitance of excitatory and inhibitory short-term plasticities in a PEDOT:PSS OECT.¹²⁶ Owing to the distinctive volumetric capacitance (C^*) and rapid electrochemical doping process (~ 0.4 ms) of OECTs, the dynamical reconfiguration between the excitatory and inhibitory responses with 10 mV stimulus resolution and multilevel synaptic strength was realized by controlling the doping degree of PEDOT:PSS, without performing operations or introducing additional modulation terminals. High frequency input signals (50 Hz) could induce a strong suppression/potentiation effect to filter out the corresponding low/high frequency input signal, and thus, both low-pass/high-pass filtering functions can be implanted in a single synaptic device by modulating the synapse operation modes.

An enormous effort has been made in understanding the mechanism that underlies learning and memory.¹²⁸ Learning may be

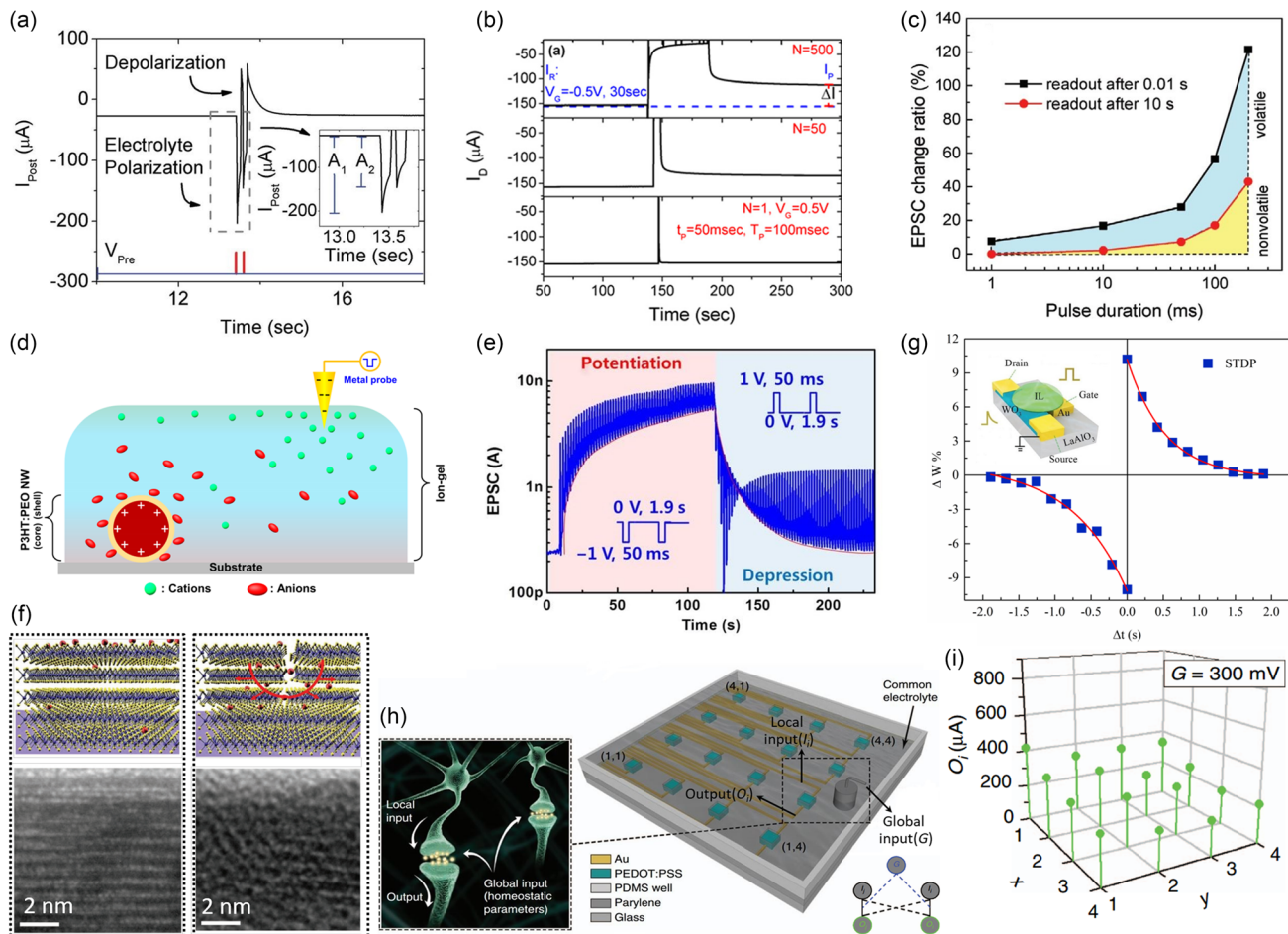


FIG. 3. (a) PPD effect in PEDOT:PSS-based synaptic OECTs.¹⁰⁹ Reproduced with permission from Gkoupidenis *et al.*, *Adv. Mater.* **27**, 7176 (2015). Copyright 2015 Wiley-VCH. (b) STM to LTM transition as a function of the pulse training sequence.¹³² Reproduced with permission from Gkoupidenis *et al.*, *Appl. Phys. Lett.* **107**, 263302 (2015). Copyright 2015 AIP Publishing LLC. (c) STM to LTM transition as a function of pulse duration ($V_p = 2.5$ V).¹⁰² Reproduced with permission from Yang *et al.*, *Adv. Mater.* **29**, 1700906 (2017). Copyright 2017 Wiley-VCH. (d) Schematic of the ion gel-gated P3HT core-sheath nanowire synaptic transistor. (e) LTP and LTD triggered by 60 negative and 60 positive pulses.¹⁰⁸ Reproduced with permission from Xu *et al.*, *Sci. Adv.* **2**, e1501326 (2016). Copyright 2016 AAAS. (f) Zoomed-in HRTEM image and schematic illustrations of Li^+ adsorption on the surface (left, STP) and Li^+ intercalations into the van der Waals gaps (right, LTP).¹⁰³ Reproduced with permission from Zhu *et al.*, *Adv. Mater.* **30**, 1800195 (2018). Copyright 2018 Wiley-VCH. (g) Asymmetric STDP function implemented in the WO_3 -based synaptic EGTs.⁶¹ The inset shows the schematic representation of the synaptic EGTs. Reproduced with permission from Yang *et al.*, *Adv. Mater.* **30**, 1801548 (2018). Copyright 2018 Wiley-VCH. (h) Schematic of the configuration of the array of PEDOT:PSS-based synaptic OECTs and principle of the global input. (i) Spatial maps show that the global input forces a global restriction on every output.⁷⁶ Reproduced with permission from Paschalis *et al.*, *Nat. Commun.* **8**, 15448 (2017). Copyright 2017 Springer Nature Publishing.

described as the mechanism by which new information about the world is acquired and memory as the mechanism by which that knowledge is retained. At the cellular level, it has been revealed that long-term potentiation consists of distinct phases involving different molecular mechanisms.¹²⁹ The storage of long-term memory is associated with gene expression, *de novo* protein synthesis, and formation of new synaptic connections.⁸ At the device level, ion penetration into the channel is the identifying characteristic of OECTs, resulting in an operation mechanism that is distinctly different from EDLTs. Given the inherent reversibility of ion injection/extraction in/from the loose bulk of the channel volume, the implementation of long-term memory properties in conjugated polymer-based OECTs is still challenging. Generally, the nonvolatile conductance tuning was obtained in

synaptic OECTs by modulating the electronic structure of channel materials.^{58,130,131} Gkoupidenis *et al.* used a poly(tetrahydrofuran) (PTHF)-based PEDOT derivative (PEDOT:PTHF) as the OECT channel gated with an aqueous KCl electrolyte (0.1 M).¹³² When a high reduction potential was applied, the polymer structure PEDOT:PTHF underwent a structural collapse and an opposite polarity oxidation potential was required for the reversal of this conformational change.¹³³ As a result, the PEDOT:PTHF OECTs exhibited a nonvolatile phenomenon and could operate either in the STM or LTM regime, depending on the number of training pulses [Fig. 3(b)]. The amplitude of PSCs persisted a permanent increase in synaptic efficacy after the repetitive stimulation, resulting in long-term phenomena. The coexistence of a STP function upon an LTM state is similar to biological

memory and supports merged processing and storage capabilities in a single device level. Gerasimov *et al.* reported an evolvable synaptic OECT by electropolymerizing a self-doped conjugated monomer sodium 4-(2-(2,5-bis(2,3-dihydrothieno[3,4-b][1,4]dioxin-5-yl)mthiophen-3-yl)ethoxy)butane-1-sulfonate (ETE-S) as the channel and 0.01 M NaCl as the electrolyte, which exhibited STM and LTM functionalities.⁶⁰ The p-type PETE-S could operate in the hybrid accumulation-depletion mode, enabling the mimicking of short-term potentiation (STP) and depression (STD) when applying a small negative/positive V_G below 0.3 V with short pulse duration (100 ms). However, the LTP and LTD properties were attained by electropolymerization and electrochemical overoxidation of the channel material under 30 V_G spikes of -0.5 V and -2 V (1 s), respectively. Classical conditioning was also demonstrated by connecting a preformed PETE-S resistor and an evolvable OECT.

The STM to LTM transition has been extensively studied in EDLTs and can be accomplished by modifying the ionic gating effects from ideal electrostatic coupling (surface accumulation and without interfacial electrochemical processes) to electrochemical reactions (ion intercalation) through higher V_p and/or longer t_p gate presynaptic spikes [Fig. 3(c)].^{61,102,103,134} Xu *et al.* reported organic core-sheath nanowire artificial synapses that were gated with an ion gel composed of a poly(styrene-block-methyl methacrylate-block-styrene) (PS-PMMA-PS) triblock copolymer and 1-ethyl-3-methylimidazolium bis(trifluoromethyl sulfonyl) imide [EMIM]⁺[TFSI]⁻ ionic liquid [Fig. 3(d)].¹⁰⁸ The p-type poly(3-hexylthiophene) (P3HT) core was printed and wrapped with a polyethylene oxide (PEO) sheath. The nanowire printing technique could precisely define the channel length down to 300 nm, ensuring that the synaptic device has a low energy consumption down to ≈ 1.2 fJ per spike. When the synaptic transistor was stimulated by 30 presynaptic spikes (-1 V or 1 V, 50 ms), the anions/cations that accumulating near the nanowire would penetrate into the P3HT core through the PEO sheath and gradually increased/decreased the charge carrier density in the channel. Due to the PEO sheath, the spontaneous release of the trapped ions in the P3HT nanowire was slow, and this restricted mobility induced LTP or LTD. As shown in Fig. 3(e), the organic nanowire-based synaptic transistor operated in an analog fashion with gradual but nonlinear conductance changes. However, a large range of linearly and symmetrically programmable conductance states are required to avoid complex programming schemes in large arrays and to facilitate near-ideal training and inference accuracy in neural network simulations.^{131,135} In this regard, Yang *et al.* reported a polymer electrolyte PEO:LiClO₄ gated synaptic transistor based on 2D van der Waals (vdW) layered WSe₂ that could biorealistically emulate both STP and LTP.¹⁰³ As shown in Fig. 3(f), the high-resolution transmission electron microscopy (HRTEM) characterization supported that when a gate pulse (5 V, 50 ms) was applied, the Li⁺ ions were adsorbed to the surface of the 2D materials. Ions diffused back into the ion gel after the removal of the gate bias, leading to the STP property. In contrast, when the Li⁺ ions got intercalated into the vdW material after the application of 100 gate pulses (5 V, 50 ms), they could not be liberated spontaneously after removing the gate bias, and hence, backward diffusion of the ions was retarded, leading to the LTP behavior. Because the STP property was dominated by surface adsorption, the short-term synaptic response was related to the effective area of the vdW channel, whereas it was insensitive to the layer number of the vdW material. The long-term synaptic activity could be

effectively manipulated by tailoring the diffusion dynamics by varying thicknesses and structures of the vdW materials, producing LTP and LTD functionalities with enhanced linearity, symmetry, and reproducibility. Ge *et al.* reported concomitant STP and LTP behaviors using the insulator-metal transition mechanism in an n-type tungsten oxide (WO₃) synaptic transistor, which was gated with an ionic liquid of N,N-diethyl-N-(2-methoxyethyl)-N-methylammonium bis-(trifluoromethylsulfonyl)-imide [DEME]⁺[TFSI]⁻.⁶¹ When a positive V_G (0.6 V, 70 ms) was applied, DEME⁺ ions accumulated at the ionic liquid (IL)/channel interfaces to form EDLs and induced additional electrons in the channel. Once V_G was removed, cations and anions in the ILs relaxed and mixed together in short time, leading to volatile phenomena. The results of X-ray photoelectron spectroscopy (XPS), Raman spectroscopy, transmission spectroscopy, and secondary ion mass spectrometry (SIMS) clarified that when V_G (1.8 V, 210 ms) was higher than the threshold value of the hydrolysis reaction (V_T), the trace water molecules contained in the ILs could dissociate into protons (H⁺) and hydroxyls, both of which had smaller ion sizes and relatively high chemical reactivity.¹⁰² The protons then penetrated into the WO₃ channel, resulting in the formation of a stable metallic H_xWO₃ phase and the nonvolatile resistance state. The synaptic potentiation and depression could be reproduced by consecutive positive (1.8 V, 210 ms) and negative spikes (-1 V, 210 ms), respectively. A typical asymmetric STDP was obtained in this WO₃ synaptic transistor, which was induced by temporal correlations of pre- and postsynaptic spikes [Fig. 3(g)].

Various mechanisms have been adopted to implement the nonvolatility and modulate the functional regions from STP to LTP, such as electrostatic coupling, electrochemical doping/dedoping, charge trapping/detrapping, ferroelectric polarization, and phase transformation (electropolymerization, insulator-to-metal, semiconductor-to-metal, and amorphous-to-crystalline).^{60,61,98,136} Note that most of the reported LTP is based on large structural transformations in channels, resulting in high write noises and even irreversible electrochemical doping.¹³⁴ If operated in their subthreshold regime (e.g., with the use of low amplitude and/or narrow width input pulses), the nonvolatile transistors can practically only show STM dynamics without affecting the LTM. However, nonvolatile neuromorphic devices with write-erase ability and structural stability are highly desired. For example, Fuller *et al.* reported an all solid-state, nonvolatile electrochemical transistor. In this device, a negative gate voltage induced the intercalation of Li⁺ dopants into the channel of Li_{1-x}CoO₂.¹³⁷ The channel then undergoes an insulator-to-metal transition with nearly six orders of magnitude increase in electronic conductivity. A positive gate voltage could reintercalate Li⁺ and return the channel to its initial conductivity. This process was highly reversible and without large structural transformations. In a device based on the conductive polymer PEDOT:PSS, a similar LTP behavior was demonstrated.⁵⁸ In this example, the device resembles an electrochemical battery, where ionic charges (protons) can move through the electrolyte that separates the two organic electrodes, while electronic charges move through the electronic circuit. This results in enhanced state stability and analog tuning. To further enhance the state and cycle stability, smart material design and the definition of the number of separable states have to be taken into account.¹³⁰

Hebbian plasticity alone through potentiation and depression is expected to be insufficient to explain activity-dependent development

because it tends to destabilize the activity of neural circuits (i.e., higher temporal correlation between pre- and postsynaptic signals leads to a higher coupling between neurons, with no upper limit).¹³⁸ Homeostatic plasticity is another important function that is believed to stabilize the neuronal activity that was induced by the positive-feedback nature of Hebbian plasticity.¹³⁹ Homeostatic plasticity mechanisms include global changes in synaptic strengths and changes in neuronal excitability. Due to the fact that biological neural networks are immersed in a common electrolyte environment, global factors of this environment are forcing specific normalization functions that regulate the overall network behavior.¹³⁹ Gating OECTs with electrolytes offers a straightforward way to emulate homeostatic regulation, a phenomenon that is not easily accessible with other solid-state technologies.^{76,140,141} Gkoupidenis *et al.* demonstrated the global control of a whole array of PEDOT:PSS-based OECTs that were immersed in a 0.1 M NaCl electrolyte [Fig. 3(h)]. The weights of these individual artificial synapses could be modulated globally by the voltage applied on the electrolyte and by its ion concentration, in the way that was analogous to homeostasis. The synchronization of I/O transmission could be reproduced in this system [Fig. 3(i)]. Additionally, the electrolyte established soft connections between individual devices (grids) without hard connectivity (i.e., physical wiring). It was also shown that the output (O_i) of these grids could be synchronized by a global oscillatory input despite the fact that individual local inputs (I_i) were stochastic and independent.¹⁴¹ The synchronization effect was more pronounced at its amplitude extrema and high frequency of the global oscillatory input. This global temporal coupling resembled well the phase locking of neurons to brain oscillations, leading to a functional type of connectivity found in brain oscillations (i.e., binding through synchrony).

B. Biofriendly materials and mechanically flexible electrolytes

In recent years, flexible, wearable, and implantable electronics are attracting increasing interest for healthcare and biomedical applications.¹⁴² In addition, the use of biocompatible and biodegradable materials in electronic devices can be an important trend in the development of green electronics.¹⁴³ Compared with metal-oxide semiconductors, biofriendly conjugated polymers (CPs) as channel materials of EGTs have received growing attention in flexible neuromorphic platforms for their advantages such as chemical tunability, low cost, mechanical flexibility, and compatibility with printing and roll-to-roll processes.¹⁴⁴ Conjugated polymers can not only transport ions but also transport holes (p-type; popular examples include PEDOT:PSS,^{145,146} PANI,¹¹³ P3HT,^{147,148} and poly(2-(3,3'-bis(2-(2-methoxyethoxy)ethoxy)ethoxy)-[2,2'-bithiophen]-5-yl)thieno [3,2-b]thiophene) [p(g2T-TT)]^{149,150} or electrons [n-type, such as p(gNDI-gT2),¹⁵¹ P-90,¹⁵² and poly(benzimidazobenzophenanthroline) (BBL)¹⁵³]. The simulation of synaptic functions in organic EGTs has extended the functionality into E-skins, artificial afferent nerve, etc., which highly benefits from the mixed conductivity and biocompatibility features of conjugated polymers.^{144,154,155}

Biocompatible and biodegradable electrolyte materials are also highly recommended for green electronics since the electrolyte is the integral part of an EGT. Electrolyte materials consist of ionic liquids (ILs),^{61,156} ion-gels,^{92,157,158} polyelectrolytes,¹⁵⁹ polymer electrolytes,^{100,103,160} aqueous salts [e.g., NaCl, KCl, and phosphate buffered saline (PBS) solution], and even water.¹⁶¹ Among them, proton-rich

biopolymers are attracting growing interest for solid-state electrolytes of green and flexible synaptic transistors since the transport of protons is found in many natural phenomena such as muscle contraction, taste receptor cells, and mammalian brain.^{162,163} Typical biopolymer electrolytes that have been used include polysaccharides (chitosan,^{164–167} sodium alginate,¹⁶⁸ pectin,¹⁶⁹ and starch¹⁷⁰), cellulose (lignin¹¹⁴), and proteins (albumin¹⁷¹). Shi *et al.* used chicken albumen as the electrolyte film in n-type IZO-based synaptic EGTs.¹⁷¹ According to the leakage and electrochemical impedance spectroscopy (EIS) measurements [Fig. 4(a)], the hydrated albumen film was an electron insulating but ionic conducting electrolyte with a maximum leakage current density of 5×10^{-7} A/cm² at -0.02 MV/cm and a high proton conductivity (σ) of $\sim 3.7 \times 10^{-4}$ S/cm. The ionic conductivity was mainly attributed to the migration of protons induced by the amino acid interaction with H₂O. Protons could move along the hydrogen-bond network following the Grothuss mechanism. Thus, it was necessary to maintain a certain water content for the fabrication and characterization of the biopolymer electrolyte-based synaptic transistors. As shown in Fig. 4(b), the specific capacitance increased with the decreasing frequency and reached the maximum value (>1.0 μ F/cm²) at 1.0 Hz due to the formation of huge interface EDL capacitance. Note that at a higher voltage level of >2.0 V and a frequency of <10 Hz [Fig. 4(c)], the mobile protons penetrated across the albumen/IZO interface and reacted with IZO, resulting in surface hydrogenation and an increase in nonvolatile IZO conductance. For the biodegradable electronics, Guo *et al.* reported a starch-based electrolyte for indium-tin-oxide (ITO) synaptic EGTs.¹⁷⁰ Starch is an environmentally friendly and naturally abundant polymeric carbohydrate. During the gelatinization process, water molecules are bound to the starch chain network. The proton conductivity (σ) of the ~ 14 μ m thick starch film was estimated to be $\sim 2.6 \times 10^{-3}$ S/cm. The proton related EDL capacitance was ~ 1.6 μ F/cm² at 1 Hz. Both short-term and long-term synaptic plasticities were mimicked under voltage spikes of 0.5 V (10 ms) and 4 V (600 ms), respectively. Due to the water solubility of the starch film, the devices could easily be dissolved in DI water after soaking for 60 s [Fig. 4(d)].

In addition to the nontoxicity and biodegradability, biopolymer-based electrolyte films have the advantage of being active flexible substrates in forming or conforming to complicated textures and shapes.¹⁷² Liu *et al.* reported a freestanding chitosan membrane to act as both the electrolyte and the flexible substrate in the IZO EGTs.¹⁶⁴ The 100 μ m chitosan membrane was able to form transparent pinhole-free conformal coatings with a surface strain (ϵ) of 0.5% at 10 mm bending radius. Since the chitosan membrane is a three-dimensional proton conductor, when a positive presynaptic spike was applied on the in-plane gate, protons were driven laterally and accumulated at the chitosan/IZO channel interface [Fig. 4(e)]. The drain current was increased due to the accumulated electrons by the proton/electron electrostatic coupling effect. Figure 4(f) shows the paired pulse facilitation (PPF) behavior as a function of the interval between two successive presynaptic spikes (1.5 V and 50 ms) for the freestanding synaptic transistor. The PPF ratio decreased gradually with increasing Δt , and a maximum PPF value of $\approx 222\%$ was obtained at $\Delta t = 10$ ms. The distance between the laterally coupled gate electrodes and the channel layer was shown to play a key role in the operation frequency. For example, the PPF value decreased much slower with a larger gate-to-channel distance due to the fact that longer diffusion time was needed for the protons to relax back to the balanced state in the case

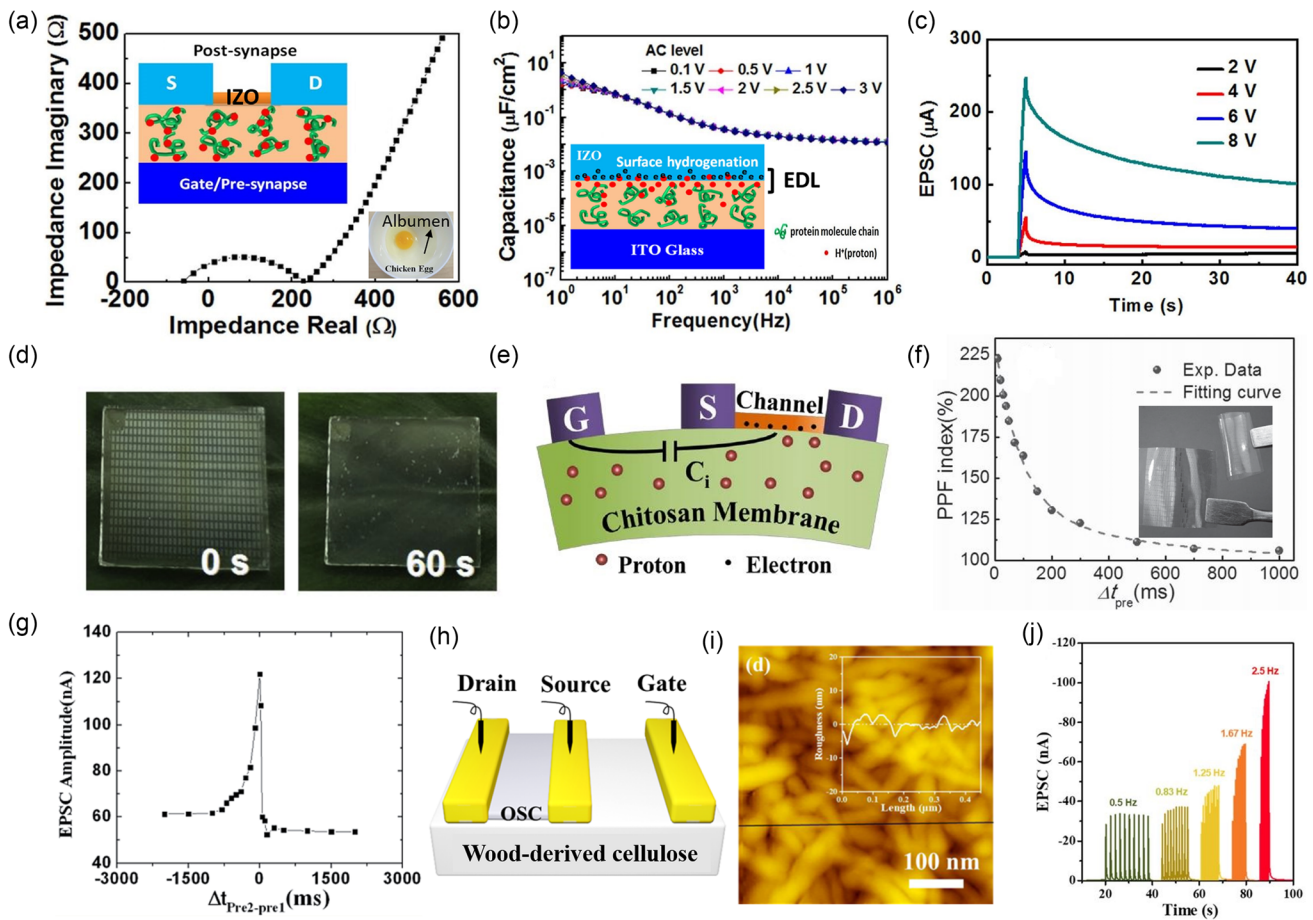


FIG. 4. (a) A typical Nyquist plot of the albumen film. The inset shows the diagram of the schematic diagram of the albumen-gated synaptic EGT. (b) Specific capacitance of the albumen film as a function of frequency under different AC potentials. The inset shows the schematic diagram of the IZO/albumen interface hydrogenation process under high bias potential. (c) STM to LTM transition as a function of pulse amplitudes ($t_p = 1$ s).¹⁷¹ Reproduced with permission from Wu *et al.*, *Sci. Rep.* **6**, 23578 (2016). Copyright 2016 Springer Nature Publishing. (d) Dissolution processes of the starch electrolyte gated ITO synaptic transistors on a glass substrate in de-ionized water at room temperature.¹⁷⁰ Reproduced with permission from Guo *et al.*, *Org. Electron.* **61**, 312 (2018). Copyright 2018 Elsevier. (e) Schematic diagram of the chitosan-gated IZO freestanding synaptic transistor. (f) PPF index as a function of presynaptic spike interval (Δt) between two successive presynaptic spikes (1.5 V, 50 ms). The inset shows the optical image of the freestanding synaptic transistors.¹⁶⁴ Reproduced with permission from Liu *et al.*, *Adv. Mater.* **27**, 5599 (2015). Copyright 2015 Wiley-VCH. (g) Spatiotemporally correlated EPSC as a function of $\Delta t_{pre2-pre1}$ between the two presynaptic spikes (0.5 V and 1 V, 20 ms).¹⁶⁵ Reproduced with permission from Wu *et al.*, *J. Mater. Chem. C* **2**, 6249 (2014). Copyright 2014 Royal Society of Chemistry. (h) Schematic of WCN-gated C8-BTBT freestanding synaptic transistors. (i) AFM image of WCNs. (j) A high-pass filtering behavior in the C8-BTBT synaptic transistor.¹¹⁴ Reproduced with permission from Dai *et al.*, *ACS Appl. Mater. Interfaces* **10**, 39983 (2018). Copyright 2018 American Chemical Society.

of a larger migration distance.¹⁷³ Due to the lateral coupling property, the freestanding solid-state electrolyte has been proven suitable for coplanar-gated transistors to emulate temporal summation functions.¹⁶⁵ As can be seen in Fig. 4(g), the obtained EPSC was asymmetrical with respect to the time interval between the temporally correlated spikes from two separate gate inputs. Huang *et al.* reported the use of wood-derived cellulose nanopapers (WCNs) as a freestanding electrolyte in C8-BTBT-based synaptic transistors [Fig. 4(h)].¹¹⁴ The as-fabricated $30 \mu\text{m}$ WCNs were composed of densely packed nanosized fibers with around 1 nm roughness [Fig. 4(i)]. This smooth active substrate exhibited high transparency (close to 90%) in the visible-light region. Freestanding WCNs were rich in hydrogen bonds and thus able to absorb moisture from the air and thus introduce protons into WCNs. The active film exhibited an ionic conductivity of

$7.3 \times 10^{-3} \text{ S/cm}$ and a high laterally coupled effective capacitance of 18.65 nF/cm^2 at 30 Hz. The spatial summation function was reproduced in the C8-BTBT synaptic transistors with dual coplanar-gates, which showed a sublinear integration. The lateral effective capacitance and the dendritic integration effect were tuned by controlling the distance of the in-plane gates. A high-pass filtering effect was also simulated in Fig. 4(j), and the increase in the presynaptic spike frequency would induce a strong EPSC amplitude increase.

C. Spatially correlated functions

In the brain, information processing is spatiotemporal. The ability of the human brain to convert input information from multipathways into specific output patterns is important for learning, memory,

executing event-driven behaviors, and enabling parallel computations.¹⁷⁴ Dendritic integration plays an important role in information transformation including the addition of nonsimultaneous unitary events (temporal summation) and addition of unitary events occurring simultaneously in separate regions of the dendrite (spatial summation).¹⁷⁵ An electrolyte shows frequency sensitivity and bulk ion conductivity, enabling the laterally gated transistor configuration in which both the gate electrodes and a source-drain channel are patterned concurrently in one plane, decreasing fabrication complexity. Spike pulses applied on multi-in-plane gates are in analogy to parallel synaptic inputs from various dendritic positions. Both the gate-to-channel distance (dendrite to postsynapse) and gate electrode area contribute to the change in the synaptic weight.^{77,100} Thus, electrolyte-gated neuromorphic transistors with lateral multigates would be helpful for realizing spatially correlated functions and advance the capability of neuromorphic performance on single synaptic devices. Interesting spatiotemporal information processing functions such as spatial co-ordination and visual orientation recognition,^{77,100,111,127,161,176} visual detection,¹⁷⁷ sound location functionality,¹⁷⁸ spiking logic response,^{99,110,164} spatial summation,^{114,179} and classical conditioning¹⁸⁰ have been demonstrated.

Orientation selectivity is a broadly investigated phenomenon in the primary visual cortex.^{181,182} Gkoupidenis *et al.* demonstrated this function in a PEDOT:PSS-based OECT array with 3×3 coplanar Au gate electrodes [Fig. 5(a)].⁷⁷ An enhanced current response I_0 (i.e., PSC amplitude) was obvious for the gates that are closer to the drain electrode, which was attributed to the decrease in the electrolyte resistance (R_E) for smaller gate-drain electrode distances (d). Similar to the current response I_0 , inhomogeneity toward the drain electrode was also evident in the relaxation time (t_R) mapping. The closest to the drain, gate electrode ($x=1, y=1$) resulted in the lowest t_R value. This spatial inhomogeneity in PSC could thus be used for implementing the orientation selectivity function. As shown in Fig. 5(b), the variable orientation could be created by superimposing eight gate pulses at gate electrode 0 and another gate electrode x ($x=1-6$), simultaneously.¹¹¹ The spatial orientations of the input pulse were defined by the angle range from 0° to 180° . Figure 5(c) shows the polar diagram of the EPSCs for different spatial orientations of the input pulse for this ion-gel gated P3HT synaptic transistor. The average peak EPSC was gradually increased with the orientation angle changed from 0° to 50.2° or from 180° to 129.8° , which was similar to the orientation tuning curve in the primary visual cortex. The maximum tuning response ($2.22 \mu\text{A}$) was obtained at the orientation angle of 129.8° , for gate electrode 5 that was the closest to the drain electrode. Neurons in the primary visual cortex respond preferentially to edges with a particular orientation. Inspired by this, a neuromorphic system with a combination of photodetectors and a multigated synaptic transistors was further developed to mimic the edge recognition function.^{161,176,179} As shown in Fig. 5(d),¹⁶¹ a square panel with five pairs of black-white grating patterns was moved along the y axis in the yz plane. The orientation angle (θ) was defined as the angle between the z axis and the grating orientation. The coordinate of the photodetector is $(x, 0, 0)$, and the coordinate of the panel center was $(0, y, 0)$. Each time the edge of the grating pattern moved across the coordinate origin, it was detected by the photodetector, and the processing circuit would provide a voltage pulse (0.5 V, 10 ms) to the presynaptic terminal of the aqueous solution gated n-type indium-gallium-zinc oxide (IGZO) synaptic transistor. Figure 5(e) shows that when the maximum value of EPSC was

obtained at the orientation of 0° , ten presynaptic spikes induced by ten edges were triggered successively. Orientation selectivity was shown to be dependent on the ionic conductance of the aqueous electrolyte. Besides, the alcohol solution gated synaptic transistor demonstrated the highest degree of orientation selectivity since the delivery of hydronium and hydroxyl ions was inhibited (facilitated) by alcohol molecules (salt ions). An individual multigate neuromorphic transistor has also been used for object detection. Wan *et al.* designed a visual system for emulating the Lobula Giant Movement Detector (LGMD) neuron.¹⁷⁷ The system was constructed by a 20×20 photoreceptor array connecting to the multiple in-plane gate arrays of the IZO neuromorphic transistor in a one-to-one correspondence [Fig. 5(f)]. Proton conducting graphene oxide (GO) electrolytes were fabricated on graphene/poly(ethyleneterephthalate) (PET) substrates. Both of the square object and the photoreceptor array were parallel to the xy plane with the center coordinates of $(0, 0, z_0)$ and $(0, 0, z_a)$, respectively. The gray dashed box denotes the image of the object in the photoreceptor array, and the edge movement thus could be detected by comparing the difference between the successive images. The excitatory stimuli (0.5 V, 1.0 ms) were triggered and then sent to the corresponding presynaptic terminals (gates) of the neuromorphic transistor once the object edge was detected by using a photoreceptor. Three object approaching modes (toward, away, and parallel) to the photodetector array were then distinguished according to the EPSC dynamics.

The computing functions in the neural network are based on synaptic integrations. The spatial summation has been leveraged to reproduce Boolean logic operations. As shown in Fig. 5(g), two types of logic “AND” and “YES_{V₂}” were constructed, respectively, by changing the applied gate voltage drop across the channel that was controlled by the area of gate electrodes. The input 10 ms voltages of 0 and 1.0 V were defined as 0 and 1, respectively. The integrated EPSC amplitude was defined as the output, and the threshold value was set to 750 nA. For the same electrode area, the EPSC amplitude was larger than the threshold line only when input signals were “11,” which indicated the AND logic. When the area of G_2 was ≈ 2.5 -fold larger than that of G_1 , the capacitance of the G_2 -electrolyte interface would be larger to induce the efficient EDL gating. As long as input V_2 is 1, the output EPSC amplitude was larger than the threshold value, which indicated the YES_{V₂} logic. Besides, the “OR” logic, synaptic weight regulation, and coincidence detection could be achieved by introducing a modulatory terminal (G_m), and thus, the network functionalities can be enriched.^{110,164} The spatial summation effect was also demonstrated with two spatial isolated presynaptic inputs in GO-coupled synaptic transistors [Fig. 5(h)].¹⁷⁹ When the input spikes were first triggered individually and then simultaneously on two in-plane gates (G_1 and G_2), the three EPSCs can be obtained. The red and blue curves were the EPSCs (A_1, A_2) triggered by single presynaptic spikes (V_1 and V_2) ranged from 0.2 to 1.4 V on G_1 and G_2 , respectively. The expected sum (S_E , green dashed curves) was defined as the arithmetic sum of two individual EPSC responses ($A_1 + A_2$), and the measured sum (S_M , black curves) was the EPSC stimulated by the two simultaneously triggered spikes. Summation would be expected to range from sublinear to superlinear depending on the stimulus intensity of the individual excitatory postsynaptic potentials (EPSP). Figure 5(i) shows that such spatial summation was nearly linear for low spike voltages. A linear summation model has been postulated to facilitate coincidence detection by cortical neurons.¹⁸³ Strong superlinear for intermediate

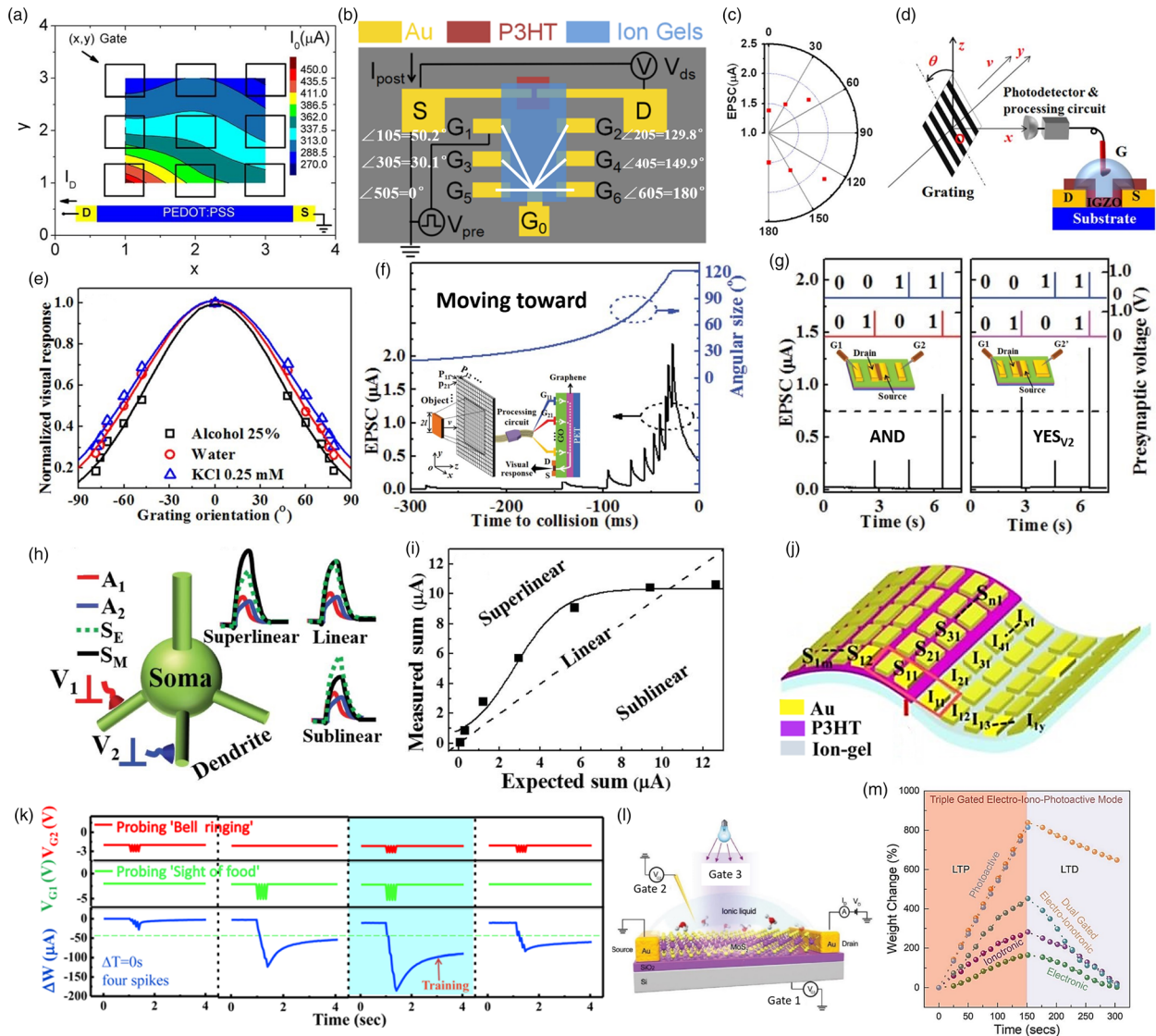


FIG. 5. (a) Spatial mapping the resulting amplitude I_0 of the IPSC. Each (x, y) gate electrode was pulsed separately (0.3V, 50 ms).⁷⁷ Reproduced with permission from Gkoupidenis *et al.*, *Sci. Rep.* **6**, 27007 (2016). Copyright 2016 Springer Nature Publishing. (b) Schematic illustrations of the ion gel-gated P3HT synaptic transistor with a multi-plane-gate structure. (c) Polar diagram of the EPSCs for different spatial orientations of the input pulse.¹¹¹ Reproduced with permission from Qian *et al.*, *Appl. Phys. Lett.* **110**, 083302 (2017). Copyright 2017 AIP Publishing LLC. (d) A schematic diagram showing the measurements for the orientation tuning experiment. (e) The normalized gain of EPSC responses plotted as a function of the orientation angle for the solution-gated IGZO synaptic transistor.¹⁶¹ Reproduced with permission from Wan *et al.*, *ACS Appl. Mater. Interfaces* **8**, 9762 (2016). Copyright 2016 American Chemical Society. (f) The EPSC output of the visual system recorded in response to an object when it moves toward the photoreceptor array. (g) Input–output characteristics of the AND and YES_{V2} logics from the two combinations of presynaptic input terminals.¹⁷⁷ Reproduced with permission from Wan *et al.*, *Adv. Mater.* **28**, 5878 (2016). Copyright 2016 Wiley-VCH. (h) The schematic diagram of the spatial summation with two spatial isolated synapses. (i) The measured sum (S_M) plotted as a function of expected sum (S_E).¹⁷⁹ Reproduced with permission from Wan *et al.*, *Adv. Mater.* **28**, 3557 (2016). Copyright 2016 Wiley-VCH. (j) Schematic of highly interconnected P3HT neural devices with an ion-gel membrane as both an electrolyte and a substrate.¹⁸⁰ Reproduced with permission from Fu *et al.*, *ACS Appl. Mater. Interfaces* **10**, 26443 (2018). Copyright 2018 American Chemical Society. (l) The proposed multigated architecture of analogous artificial MoS₂ synapses. (m) Controlled facilitation and depression of synaptic weights with the electroiono-photoactive multigated architecture.⁵⁹ Reproduced with permission from John *et al.*, *Adv. Mater.* **30**, 1800220 (2018). Copyright 2018 Wiley-VCH.

spike voltages and sublinear for high spike voltages were necessary for the exponential function and logarithmic function, respectively.¹⁸⁴

The nature and geometry of the gate electrode can be regarded as a key factor for designing the initial synaptic weight distribution in

the electrolyte-gated neuromorphic system. For example, classical conditioning according to the Pavlovian associative learning rule has been implemented in a multiterminal P3HT synaptic transistor.¹⁸⁰ The topology of multi-inputs to one-output was mapped with lateral gates

through solid-state ion-gel consisting of poly(vinylidene fluoride-cohexafluoropropylene) (PVDF-co-HFP) and 1-ethyl-3-methylimidazolium bis-(trifluoromethylsulfonyl)imide ($[\text{EMI}]^+[\text{TfSA}]^-$) ionic liquid [Fig. 5(j)]. Based on protonic electrochemical doping/dedoping processes at P3HT/ion gel interfaces, four types of STDP learning behaviors of Hebbian STDP, anti-Hebbian STDP, symmetrical STDP, and visual STDP were successfully mimicked on a single neuromorphic transistor. The classical conditioning was demonstrated as shown in Fig. 5(k), and four -3 V pulse signals ($t_p = 50$ ms and $\Delta t = 50$ ms) were applied to the G_2 electrode to simulate the unconditioned stimulus of “bell ringing,” which induced a smaller change in the synaptic weight value (ΔW_{peak}) compared to the defined threshold ($45 \mu\text{A}$, green dotted line), corresponding to the absence of salivary response. When four -5 V pulse signals ($t_p = 50$ ms and $\Delta t = 50$ ms) were applied to the G_1 electrode to simulate the conditioned stimulus of “sight of food,” a ΔW_{peak} value larger than the threshold was triggered, which corresponds to the salivary response. Then, four -3 and -5 V input signals were applied simultaneously to the G_1 and G_2 electrodes to simulate the training process. After training, a salivary response could be produced even with four -3 V pulse signals (bell ringing) due to the nonvolatile feature. Therefore, an effective link between the input signals applied to the G_1 and G_2 electrodes was established, demonstrating that dynamic processes of memorizing were incorporated into the gate matrix simulation.

The coexistence of multiple forms of synaptic plasticity would increase the processing capability and memory storage capacity of neuromorphic transistors.¹²⁶ With nonplanar and multigated architectures, neuromorphic EGTs could operate independently either in a pristine ionotronic mode, an electronic mode, or a photoactive mode.^{59,185,186} This configuration enables a higher order of plasticity that emulates the effects of neuromodulators such as dopamine or noradrenaline, also called heterosynaptic plasticity or three-factor learning.^{187,188} More importantly, they can operate synergistically in a dual-gated additive/subtractive mode, allowing the programming of weight changes with fine precision, with the net weight change defined by the overall capacitive coupling across the semiconducting channel.¹⁸⁹ Mathews *et al.* reported the synergistic gating effect of the electro-iono-photo in MoS_2 EGTs [Fig. 5(i)].⁵⁹ This 2D channel-based EGT addressed different levels of charge-trapping probabilities to finely tune the synaptic weights: for example, electron trapping-detrapping at the $\text{SiO}_2/\text{MoS}_2$ interface though the back-gate (Si) was responsible for the electronic-mode, ion migration-relaxation kinetics at the ionic liquid/ MoS_2 interface although the top-gate (Beryllium copper probe) accounted for the ionotronic-mode, and persistent photoconductivity though an additional light gate was used in the photoactive-mode.⁹⁴ The three modes were combined to modulate Hebbian STDP plasticity with metaplasticity and homeostatic regulation [Fig. 5(m)]. Classical conditioning was emulated using simultaneous paired stimulation of unconditioned optical and conditioned voltage pulses, resulting after the training process in associative learning.

D. Perceptron-based artificial neural network

Perceptron is a model of feedforward neural networks that comprise densely interconnected adaptive processing subunits (artificial neurons).¹⁹⁰ Perceptron-based artificial neural networks (ANNs) are intended to emulate the brain's ability to recognize and distinguish the difference between objects or meanings.¹⁹¹ A single-layer perceptron

(SLP) comprises an input layer and an output layer and can perform binary classification and thus solve linearly separable problems. The capacity of ANNs can be further enhanced by introducing additional intermediate layers (i.e., hidden layers) to construct multilayer perceptrons (MLPs). Thus, MLP networks are capable of solving nonlinear separable problems for multiclass classification.¹⁹² The performance of hardware-based ANNs has been simulated with some specific learning algorithms, mainly including the backpropagation (BP) method in which the synaptic weights are iteratively adjusted, while error back propagates from the output to input.^{137,193,194} In these simulations, the channel conductance change (ΔG) was used as the weight update for executing the learning algorithm.¹⁹⁵ Since the weights represent the synaptic strength, these processes are commonly referred to as potentiation and depression in synaptic devices, inspired from the biological terminology.¹⁹⁶ In terms of computing, cognitive tasks like pattern recognition and classification demand synaptic devices with a wide dynamic linear conductance range¹³¹ and distinguishable readout states.¹³⁰ The symmetric weight update along with low write noise and low switching voltages and currents determines the efficiency of cross-bar neuromorphic computational kernels and significantly improves the classification accuracy of backpropagation schemes.^{137,189} Owing to the decoupled input and output electrodes, as well as the symmetry between the material at the gate and the channel, synaptic EGTs can achieve gradual nonvolatile conductance changes in a range, which shows nearly linear and symmetric weight update.¹³⁷ In addition, the large specific capacitance enables low energy consumption, making EGTs as important building blocks favorable for large-scale, energy-efficient neuromorphic computing networks.

Van de-Burgt *et al.* reported the simulations of the neural network using a PEDOT:PSS-based electrochemical neuromorphic organic device (ENODE) gated with a proton conductor Nafion [Fig. 6(a)].⁵⁸ As shown in Fig. 6(b), the ENODEs showed a battery-like operation by decoupling the read and write operations with an external switch. This results in enhanced state stability and analog tuning. Hence, a low energy switching (<10 pJ for $10^3 \mu\text{m}^2$ devices) and long retention times (25 h with a 0.04% standard deviation in conductance) could be achieved simultaneously. In an ~ 1 V range, long-term potentiation and depression displaying 500 discrete and nonvolatile conductance states were obtained by applying 500 ± 1.5 mV (1 s) presynaptic pulses [Fig. 6(c)]. According to the statistical distribution of ~ 15 000 experimentally measured conductance levels, the numerical weights showed small nonlinearity (NL) and low noise ($<1\%$), meeting the requirements for high ANN training accuracy when executing updates. A three-layer network (a single-layer perceptron with one hidden layer) based ANN was simulated with the backpropagation method. The simulated ENODE-based learning circuit achieved a high classification accuracy between 93% and 97% for three types of image recognition: an 8×8 pixel image version of handwritten digits; Modified National Institute of Standards and Technology (MNIST), a 28×28 pixel version of handwritten digits; and a Sandia file classification dataset. Moreover, plastic ENODEs fabricated on PET substrates enable the potential integration of neuromorphic functionality in flexible electronic systems.

Shang *et al.* reported the simulation of handwritten digit recognition using a 2D layered α -phase molybdenum oxide ($\alpha\text{-MoO}_3$)-based synaptic EGT array gated by a PEO: LiClO_4 electrolyte [Fig. 6(d)].¹⁰¹ Voltage pulses with higher amplitudes ($>\pm 2$ V) or long duration

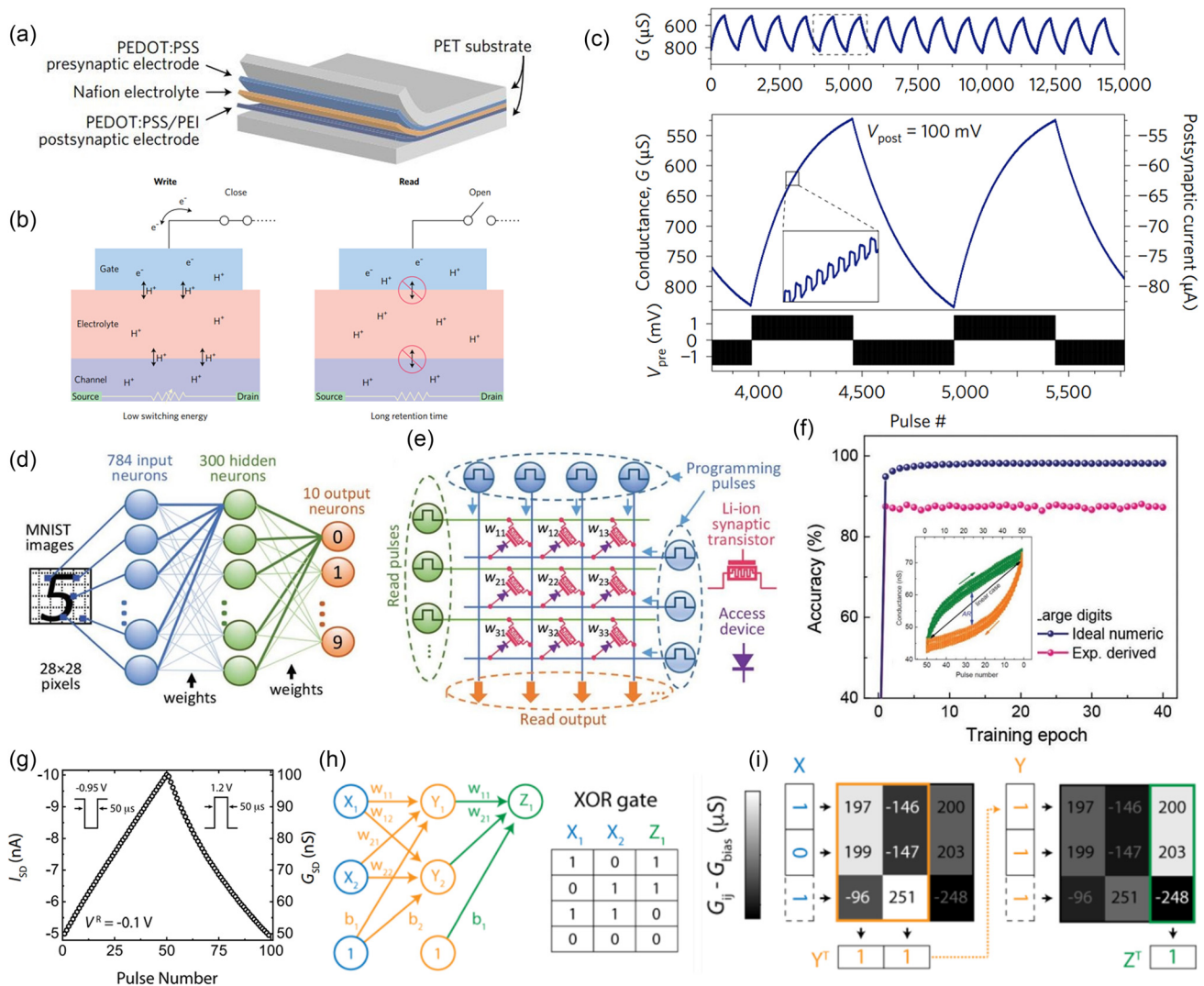


FIG. 6. (a) Schematic of the PEDOT:PSS-based flexible all solid-state neuromorphic device. (b) Schematic explaining the decoupling of the read and write operations. (c) LTP and LTD displaying 500 discrete states.^{58,214} The inset shows a zoom-in image showing the individual states. Reproduced with permission from van de Burgt *et al.*, Nat. Mater. **16**, 414 (2017). Copyright 2017 Springer Nature Publishing. (d) Schematics of a three layer (one hidden layer) neural network. (e) Schematics of a synaptic weight layer composed of voltage programmed Li-ion synaptic transistor crossbar array and access devices. (f) The recognition accuracy evolution with training epochs for the 28×28 pixel handwritten digit image. The inset shows the asymmetric ratio (AR) between the LTP and LTD and the temporal variation are calculated over 50 cycles.¹⁰¹ Reproduced with permission from Yang *et al.*, Adv. Funct. Mater. **28**, 1804170 (2018). Copyright 2018 Wiley-VCH. (g) The IFG array is mapped to a three-layer neural network used to classify XOR logic. (h) G modulation read current < 10 nA while maintaining a high signal-to-noise ratio during nearly linear and symmetric programming. (i) XOR classification function.⁷⁴ Reproduced with permission from Fuller *et al.*, Science **364**, 570 (2019). Copyright 2019 AAAS.

times (10 ms) induced the reversible intercalation of Li^+ dopants into the $\alpha\text{-MoO}_3$ lattice, forming molybdenum bronze (Li_xMoO_3) and leading to a nonvolatile ΔG . By alternatively applying 50 identical pulses (± 2.5 V, 10 ms) with 10 s interval, bidirectional analog switching was obtained, where the near-linear channel conductance was set to numerous states between 42 and 75 nS in both the LTP and LTD processes. This low conductance was promising for the application of neuromorphic networks composed of large-scale device arrays. The minimum energy consumption value for a nonvolatile ΔG was 1.8 pJ for a single pulse (2.5 V, 10 ms) event with the channel length of

$\approx 10 \mu\text{m}$. The calculated asymmetric ratio (AR) value of the synaptic transistor was as small as 0.31 ± 0.12 [the inset in Fig. 6(f)]. The cycle-to-cycle variation, i.e., write noise, was $< 12\%$ in 15 $\alpha\text{-MoO}_3$ EGT nanosheets with the channel thickness of 16.8–28.0 nm, indicating good device-to-device uniformity. Based on the experimentally measured LTPo and LTD characteristics, a three-layer network was used to perform supervised learning with BP methods. Figure 6(e) schematically shows a crossbar array. The simulated recognition accuracy approached 87.3% for a large image (28×28 pixels) of handwritten digits after 40 training epochs [Fig. 6(f)]. Park *et al.* reported a

photonic synaptic EGT with a mixed weight updating mechanism for the simulation of high-speed and low-power optic-neural networks.⁹² GO nanosheets modified with long alkyl chains (alkylated GO) were embedded as the charge-trapping sites between the ion-gel blocking gate electrolyte and the IGZO semiconducting channel. With the assistance of a light pulse, a larger conductance change ratio (G_{\max}/G_{\min}) without the degradation of the nonlinearity property was obtained and the recognition rate of MNIST training patterns was improved from 49% to 62% with 100 weight states. To further improve the recognition accuracy, more conductance states and a higher ratio of G_{\max}/G_{\min} were required through adjusting the gate pulse duration and/or amplitude but without sacrificing the linearity. A promising solution is to improve the ion capacity of the channel materials and the conductance sensitivity to doping. The nonlinear potential drop between the series resistance also affects the linearity.⁵⁸

Emelyanov *et al.* demonstrated experimentally a double hidden layered ANN to solve a nonlinearly separable task (implementation of an XOR logic gate).¹⁹⁷ In their synaptic EGTs, HCl p-doped PANI was used as the channel materials and interfaced with a PEO:LiClO₄ solid electrolyte. In the simulation, every decision boundary was performed by one neuron in the two hidden layers, and the points inside the triangle-like class corresponded to class 1, while the others corresponded to class 0. The double hidden layers allowed the perceptron to classify not only “black” (logic 0) and “white” (1) classes but also “gray” ones (some range of signal amplitude between logics 0 and 1). The possible position of decision boundaries between classes could be well defined after the learning procedure. The ability of artificial neurons to classify the “exclusive or” (XOR) logic function is a basic demonstration of the nonlinear separable task. Fuller *et al.* experimentally implemented this function into a 3 × 3 ionic floating-gate memory array (IFG).⁷⁴ The memory array was based on a PEDOT:PSS EGT connected to a selector device of two-terminal volatile conductive-bridge memory (CBM). This CBM permitted the individual addressing of redox transistors in a crossbar configuration (at the circuit level, not the physical crossbar configuration). Determined by the competition between write gate voltage (V^W) and the ON threshold V_{th} of the CBM, electron injection (extraction) through the CBM into the top PEDOT:PSS gate results in the reversible electrochemical oxidation (reduction) of the bottom PEDOT:PSS channel,⁵⁸ thereby increasing (decreasing) G . The redox transistors operated similar to a flash memory but with more than an order of magnitude lower voltage operation and weight readout <10 nA while maintaining a high signal-to-noise ratio. In addition, the devices showed finely spaced conductance levels with near-ideal analog behavior [Fig. 6(g)]. Moreover, the downscaled devices could enable a remarkable >1-MHz write-read frequency (<1 μs) for the polymer-based redox transistors. For the demonstration of the XOR logic function, an input example $X = [1, 0]$ [blue in Fig. 6(h)] was fed to the first layer of the network (orange), whereas the output $Y^T = [1, 1]$, where T denotes the matrix transpose, was sent to the last layer (green). The final output of the network correctly classified $X = [1, 0]$ as $Z^T = [1]$ according to the XOR truth table. The network was used to execute analog dot products during inference in a 3 × 3 prototype array with 100% accuracy [Fig. 6(i)]. Such highly efficient neuromorphic computers could extend ANN learning to new low-power platforms.

E. Neuromorphic sensing and biointerfacing

EGTs offer high and tunable transconductance to electrostatic potential changes and also to electrochemical phenomena, making them

sensitive for interfacing biological substances and signals.^{198,199} Inspired by the fact that nervous systems can sense, process, memorize, and classify various external stimuli, synaptic EGTs have been developed to mimic stimulisensitive artificial synapses and smart sensorimotor nerve-tronics.^{64,200} Synaptic EGTs could enable potential applications in adaptable biointerfacing, neuroinspired actuation, with long-term applications such as local diagnosis and treatment through closed-loop control of biological environment, and local control of a neural activity.⁶⁷

1. Synaptic coupling of living neurons

In the field of bioelectronics, EGTs have been interfaced with neuronal cells for biochemical signal recording and transduction of bioelectrical signals from cells and tissues.^{86,201} The amplitude of the intracellular action potential (AP) is in the range of few tens of millivolt, and it is about 2 orders of magnitude larger than the amplitude of the extracellular potential (few hundreds μV).²⁰² Owing to the large specific capacitance/transconductance, EGTs have a unique advantage of being able to sense ultralow spike amplitudes, which are in the range of intracellular APs. Functional coupling of living neurons through artificial synapses is the primary requirement for their implementation as prosthetic devices or in building hybrid networks.^{203,204} Vuillaume *et al.* reported a pentacene/AuNP-based synapse transistor interfaced with neurons [Fig. 7(a)].¹¹⁵ The NaCl-gated pentacene/AuNP EGTs showed short-term facilitating and depressing behavior when changing the input spike frequency at a low spike voltage of 50 mV. Human neuroblastoma stem cells (SH-SY5Y) were then adhered, grown, and differentiated into neurons on top of the 15 nm pentacene channel [Fig. 7(b)]. The STP response was monitored before and after cell growth. When cells differentiated into neurons for day 6 [Fig. 7(c)], there was a detectable amplitude change in the STP response.

A synapse is a biological structure, which connects two neurons enabling specific and unidirectional information flow (excitation or inhibition) from one neuron to another. In this regard, Erokhin *et al.* demonstrated this functional interface between two living neurons in rat brain slices via a PANI-based synaptic EGT [Fig. 7(d)].⁷⁵ Initially, APs evoked by suprathreshold depolarizing current injection in either neuron failed to evoke any response in another cell of the pair, indicating that this pair of cells was not connected by natural synapses in either direction. The two neurons were then connected through an electronic circuit with a PANI synaptic EGT to play the role of a synapse analog. As the resistance of the PANI channel reduced upon depolarization, the consecutive depolarizing steps and the APs in “presynaptic” cell 1 induced a gradual increase in voltage responses from the PANI EGT [Fig. 7(e), plot 3] and in “postsynaptic” cell 2 (plot 4). When the depolarizing response in cell 2 reached the AP threshold (≈ -40 mV) at sweep #113 (plot 4), cell 2 started to reliably fire APs. Moreover, the PANI synapses efficiently supported synchronized delta-oscillations in this two-neuron network. As a result, the unidirectional, activity-dependent coupling of living neurons through an organic synaptic EGT was realized. For further perspective of implantable prosthetic synapses, one must fulfill requirements such as size scaling, biocompatibility, flexibility, and stretchability of the artificial synapse.

2. Artificial sensory systems

Neuromorphic EGTs are physical computing nodes that can directly interface with analog signals from sensors, enabling the

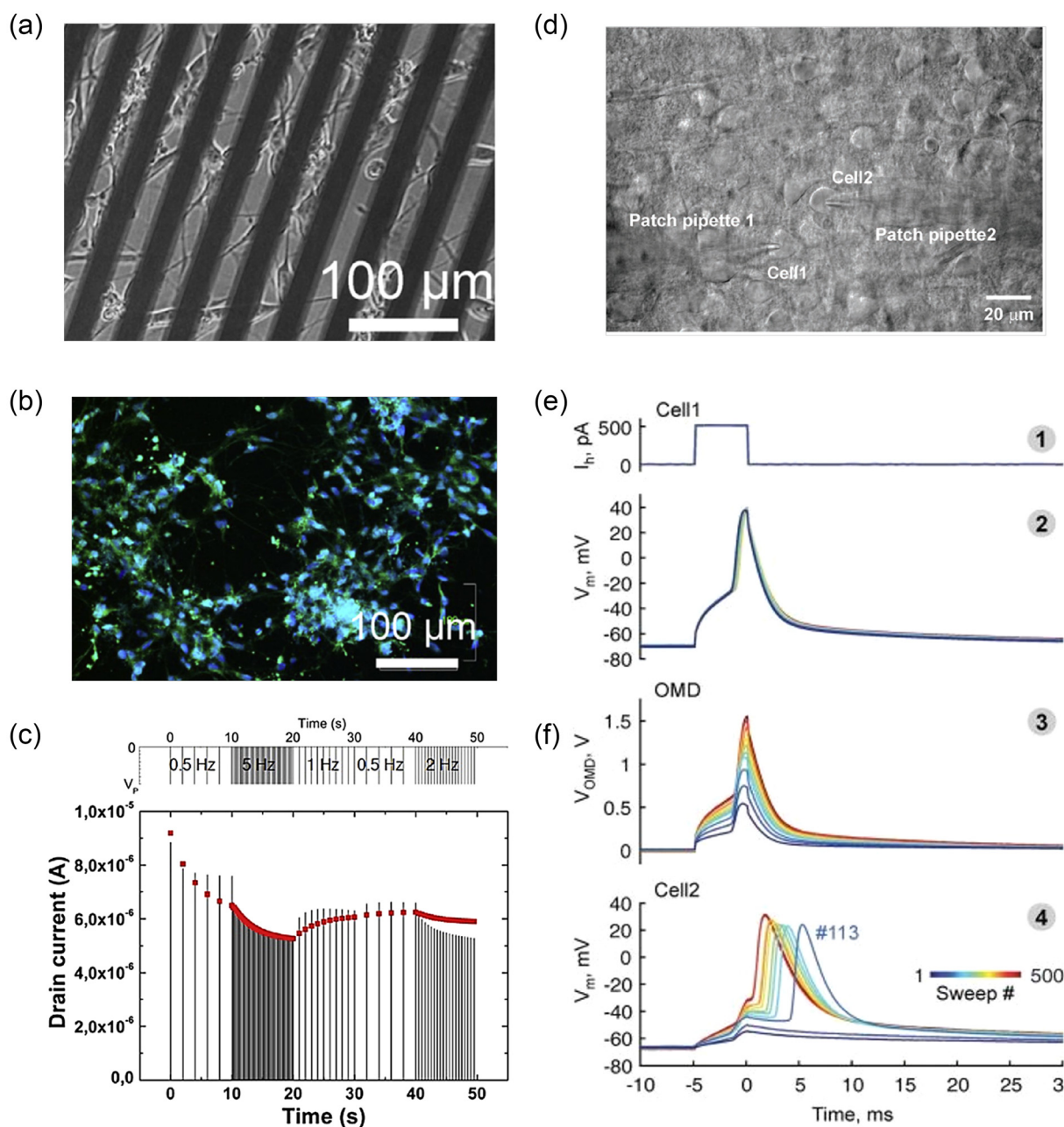


FIG. 7. (a) Optical bright field images of SH-SY5Y cells grown on interdigitated Au electrodes coated by a pentacene/AuNP thin-film. (b) Immunofluorescence images of SH-SY5Y differentiation on the synaptic EGT at day 6. (c) STP recorded as a function of electrical spike frequency (after cell differentiation).¹¹⁵ Reproduced with permission from Desbief *et al.*, *Org. Electron.* **38**, 21 (2016). Copyright 2016 Elsevier. (d) Infrared differential interference contrast microphotograph of a P7 rat brain slice with visually identified L5/6 neocortical cells (cell 1,2) recorded simultaneously. (e) Activity-dependent coupling of two cortical neurons by PANI-based synaptic EGT.⁷⁵ Reproduced with permission from Juzekava *et al.*, *Adv. Mater. Technol.* **4**, 1800350 (2019). Copyright 2019 Wiley-VCH.

efficient construction of artificial sensory systems with integrated sensing/actuation and signal processing functionalities. Since skin is the largest organ of the human body, which contains a variety of sensors, it offers the ability to perceive and interact with the surrounding environment.^{154,200} Zang *et al.* reported a dual-organic-transistor-based

tactile-perception system (DOT-TPE) with integrated sensing and neuron-like information-processing functionalities of pressure stimuli [Fig. 8(a)].²⁰⁵ The proposed DOT-TPE consisted of both a pressure-sensing organic field-effect transistor (OFET) and a signal-processing OFET using poly(diketopyrrolopyrrole-terthiophene) (PDPP3T) as

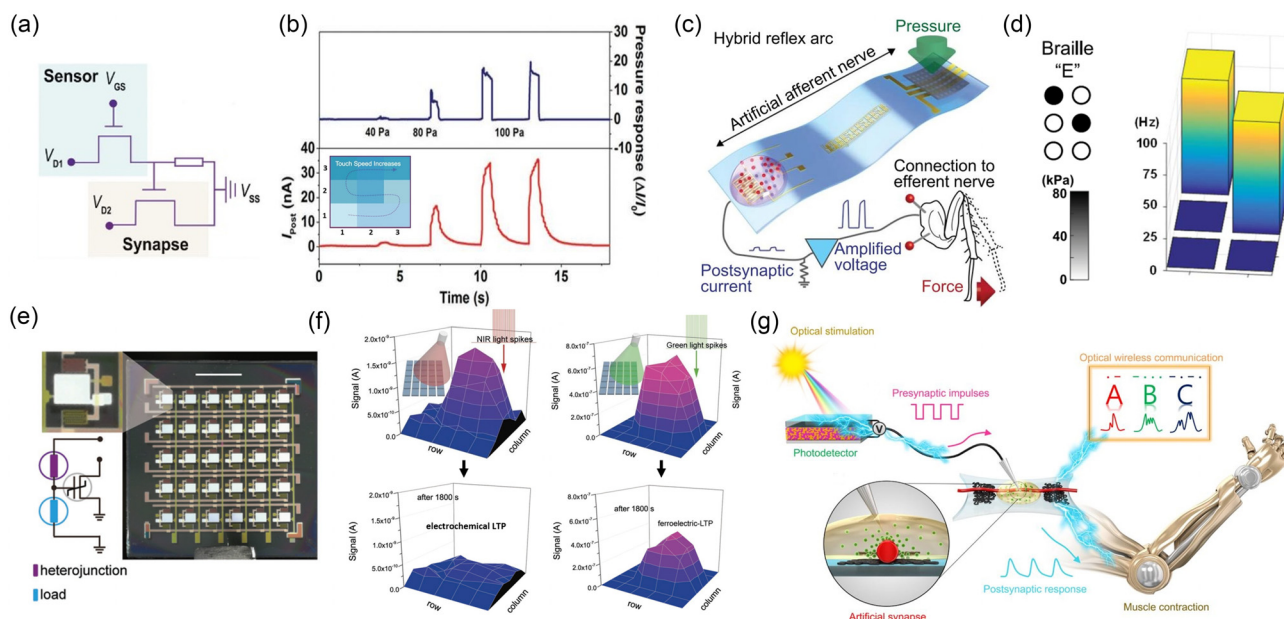


FIG. 8. (a) Equivalent electrical circuit for the DOT-TPS. (b) The relative changes in current in the pressure sensing device and the I_{post} responses of the synaptic transistor under different pressures.²⁰⁵ The inset shows the schematic illustrations of the tactile speed-perception functionality of the DOT-TPE array. Reproduced with permission from Zang *et al.*, *Adv. Mater.* **29**, 1606088 (2017). Copyright 2017 Wiley-VCH. (c) Schematic illustrations of the hybrid reflex arc made of an artificial afferent nerve and a biological efferent nerve. (d) Braille reading functionality of the artificial afferent nerve system.²⁰⁶ Reproduced with permission from Kim *et al.*, *Science* **360**, 998 (2018). Copyright 2018 AAAS. (e) Photograph of a 5×6 artificial visual-perception system array. Scale bar, 5 mm. (f) Color recognition functionality of the ferroelectric/electrochemical modulated artificial visual-perception system (Left: NIR, Right: green).¹³⁶ Top is the signal mapping immediately recorded after light exposure, and bottom is the remnant signals after 1800 s. Reproduced with permission from Wang *et al.*, *Adv. Mater.* **30**, 1803961 (2018). Copyright 2018 Wiley-VCH. (g) Schematic illustrations of the organic optoelectronic synapse and neuromuscular electronic system.¹⁰⁷ Reproduced with permission from Lee *et al.*, *Sci. Adv.* **4**, eaat7387 (2018). Copyright 2018 AAAS.

the channel layer. Chitosan was selected as the electrolyte to establish the proton–electron coupling at the semiconductor/dielectric interface. The suspended-gate OFET exhibited a high sensitivity of over 50 kPa^{-1} , which was sufficient to mimic the tactile sensing properties of human skin ($8\text{--}192 \text{ kPa}^{-1}$). The pressure sensor acted as the signal transduction element for converting the external pressure into presynaptic current pulses. Due to the instantaneous change in the potential drop across the sensing device in the DOT-TPE, the triggered presynaptic signals were processed simultaneously by monitoring the output current I_{post} of the synaptic EGT [Fig. 8(b)]. Hence, the cognitive tactile information was collected, and the increase in the strength and duration of the sustained pressure caused an increase in I_{post} . By taking advantage of the short-term synaptic facilitation function of DOT-TPE, 3×3 pixel arrays were built to mimic the tactile perception of dynamic mechanical contact. Tactile perception with comprehensive information on pressure strength and frequency was demonstrated [inset in Fig. 8(b)]. Kim *et al.* reported a bioinspired flexible organic artificial afferent nerve made of a resistive pressure sensor, an organic ring oscillator, and an ion gel-gated conjugated polymer-based synaptic transistor [Fig. 8(c)].²⁰⁶ The artificial afferent nerve could collect pressure signals ($1\text{--}80 \text{ kPa}$) and converted them into action potentials ($0\text{--}100 \text{ Hz}$) by using ring oscillators. The function of braille character reading was implanted in this artificial afferent nerve by connecting three synaptic transistors with two ring oscillators and a 2×3 array of pressure sensors [Fig. 8(d)]. The synaptic transistor integration could significantly improve the discrimination among the braille characters

with a larger Victor-Purpura distance (D_{VP}) of ~ 300 . Furthermore, the artificial afferent nerve was connected to the biological efferent nerves of a detached cockroach leg to complete a hybrid monosynaptic reflex arc. The flow of information from multiple pressure (amplitude and frequency) triggered the isometric contraction actuation of the tibial extensor muscle accordingly, indicating the successful emulation of a biological reflex arc. Recently, Chen *et al.* developed a self-powered ion gel-gated PDVT-10 synaptic transistor that mimicked the tactile synapse.²⁰⁷ This synaptic transistor was actuated by a triboelectric nanogenerator (TENG) that functioned as the tactile sensor to realize the self-powered tactile synapse. The self-powered synaptic system was able to realize AND and OR logic functions and Pavlovian conditioning. The biomimetic functionality of tactile perception systems, combined with their promising features of flexibility and large-area fabrication, represents a step forward for pressure-sensory synapses towards novel E-skins for neuromorphic sensing and actuation.

Photostimulated synapses using light as the input signals not only combine visual perception, information processing, and memory together but also provide advantages such as higher bandwidth, robustness, and potential for parallelism, which is suitable for simulating retinal neurons.^{208–210} The transduction of the color and intensity of the incident light into neural signals is a main process for visual perception. Guo *et al.* reported a ferroelectric/electrochemical modulated organic synaptic EGT for an ultraflexible, artificial visual-perception system [Fig. 8(e)].¹³⁶ A p-type copolymer poly(isoindigo-co-bithiophene) [P(IID-BT)] was used as the channel material, and bilayered

poly(vinylidene fluoride-co-trifluoroethylene) [P(VDF-TrFE)] and poly[(1-vinylpyrrolidone)-co-(2-ethylidimethylammonioethyl methacrylate ethyl sulfate)] [P(VP-EDMAEMAES)] acted as the polyelectrolytes. Besides the fundamental STP/LTP operations by electrochemical doping, the large EDL capacitance allowed P(VDF-TrFE)'s polarization switching, to achieve an extra ferroelectric LTP function with reliable nonvolatility. This synaptic EGT was integrated with an organic light-sensitive electronic component to construct an artificial visual-perception system. This light sensory system displayed an incident light intensity and frequency dependent electrochemical LTP to ferroelectric LTP transition. A 5×6 pixel array was demonstrated to allow for color recognition by converting photons from different wavelengths with identical intensity (10.80 mW/cm^2) into volatile (850 nm, 64 Hz) and nonvolatile (550 nm, 64 Hz) synaptic signals, respectively [Fig. 8(f)]. The wavelength-recognition functionality characterized by signal's degree of nonvolatility was attributed to the higher-energy green light-triggered extra ferroelectric LTP compared to the electrochemical only LTP with near infrared (NIR) irradiation. Lee *et al.* reported an optoelectronic sensorimotor synapse based on a stretchable organic nanowire synaptic transistor (s-ONWST), integrated with a photodetector and a neuromuscular system [Fig. 8(g)].¹⁰⁷ The ion gel-gated fused thiophene diketopyrrolopyrrole (FT4-DPP)-based synaptic EGT was built onto a 100% prestrained styrene ethylene butylene styrene (SEBS) rubbery substrate to introduce the stretchability. Each visible light pulse induced an output presynaptic voltage of -1.1 V from the organic photodetector to drive the s-ONWST. Spike duration and number-dependent plasticity were similar in the stretchable s-ONWST at 100% strain to those in the device at 0% strain. The optoelectronic sensorimotor system was then used for optical wireless communication. The International Morse code was coded in the form of patterns of visible light to trigger the postsynaptic potentiation of the s-ONWST, and every letter of the English alphabet was decoded according to the sum of EPSC amplitude peak values. Photoelectric neuromorphic devices are promising for the development of next-generation human-machine interface applications, soft robotics, neurobotics, and electronic prostheses.^{211,212}

IV. SUMMARY AND PERSPECTIVES

Overall, electrolyte-gated transistors are promising candidates for synaptic electronics and neuromorphic computing owing to their mixed ionic/electronic transduction, physiological environmental compatibility, mechanical/architectural flexibility, and in particular low energy consumption. Basic synaptic functions have been successfully mimicked. Unique functions arising from the inherent properties of electrolyte-gated devices are also demonstrated, including global regulation phenomena, coplanar coupling, and integration with free-standing active substrates and with living neurons, among other examples. A variety of complex tasks, such as dendritic integration, classic conditioning, pattern recognition, and sensory function, are realized in EGT-based arrays and circuits.

Currently, emulating the synapse behavior is still the main focus in this emerging field. Some challenges (reconfigurability, stability, reliability, speed, power consumption, and supporting circuitry such as selector devices) are being faced for the realization of large-scale ANNs using EGTs. The current scientific challenges and perspectives can be summarized as follows:

First, a more profound insight should be obtained into the ion transport/trapping related device physics to ensure stable and reliable neuromorphic functionalities. The most fundamental synaptic behaviors of STP and LTP are selectively induced by controlling the degree of device volatility through hybrid mechanisms. The LTP behavior suffers in many cases from challenges in large structural transformations of channel materials and/or parasitic oxidation reactions, leading to performance degradation. Novel channel materials and gating mechanisms are highly desired to maintain electronic structures for the implementation of LTP functions. Next to the simulated synaptic behavior, additional metrics should be systematically reported to evaluate the reconfiguration ability, device stability and (cycling) lifetime, and endurance.

An increase in the write-read speed and a decrease in energy consumption are needed to be able to build neuromorphic networks. The operation speed of EGTs is mainly limited to \sim kilohertz (millisecond), with the exception of a few examples, by the ion drift and diffusion in the gate electrolyte and/or the channel. Selecting gate electrolytes and channel materials with high ion mobility to shorten the ion migration time are currently suggested. The speed could also be increased by scaling down device dimensions, especially by reducing the channel and electrolyte thickness to shorten the ion diffusion distance. When the device is scaled down to sub-100 nm scale, it is possible to increase the switching speed to \sim megahertz (microsecond), which can also decrease the power consumption to the subfemtojoule level for a single spike event. Furthermore, internal ion-gated electrochemical transistors, with ions that are preloaded on the channel, have shown faster operation speeds, but their applicability in the neuromorphic device configuration should be further investigated.²¹³ Vertical configurations of transistors can also further reduce ion diffusion time, compared with a planar geometry.

Moreover, the high-density integrated circuits (ICs) of synaptic EGTs suffer from device-to-device uniformity (e.g., device noise, non-linearity, and asymmetry) and environmental dependence (e.g., humidity $> 50\%$). In addition to the optimization of thin film preparation techniques, cumulative probability and related statistics of channel conductance change (ΔG) extracted from a large amount of experimental measurements should be considered to properly simulate device nonidealities. Another issue is the requirement of a liquid electrolyte and humidity ambience in some synaptic devices. From a technological point of view, liquid gates are difficult to scale below 100 nm dimensions or to integrate with the existing solid-state circuits. From an application point of view, solid electrolyte-based synaptic EGTs show that these platforms can be downscaled for space-efficient electronic devices, while studies performed with a liquid electrolyte show their potential applications for interfacing with biology, such as human/machine interaction through neuromorphic sensing/actuation, personalized healthcare, and artificial nerves and organs.

Neural network training algorithms suitable for such device networks and supporting (external) hardware circuits should be further developed. The single-layer perceptron (SLP) model is the simplest kind of neural network and has been widely employed to implement basic training and learning. Nevertheless, more complex neural networks are required to solve demanding tasks. Toward this direction, there are only scarce attempts of hardware multilayer perceptrons with EGTs. Apart from feedforward networks, recurrent networks with EGTs are yet to be explored.

In the long-term, materials science and neuroscience should go hand in hand in order to define the computational primitives of the

brain, which are necessary for processing, and up to which level of complexity these primitives have to be emulated at the device level. This bidirectional interaction between the two disciplines should be extended beyond the functional device implementation of the synapses and neurons.

ACKNOWLEDGMENTS

F. Yan wishes to thank the Research Grants Council (RGC) of Hong Kong (Project No. C5015-15G) and the Hong Kong Polytechnic University (Project Nos. 1-ZVGH, G-YBJ0, and 1-ZVK1). H. F. Ling wishes to thank the Alexander von Humboldt Foundation for financial support via Humboldt Research Fellowships for Postdoctoral researchers. H. F. Ling also acknowledges the support of the National Natural Science Foundation of China (No. 61905121), the Natural Science Foundation of Jiangsu Province, China (No. BK20190734), and Nanjing University of Posts and Telecommunications Start-up Fund (No. NY219157). Y. van de Burgt acknowledges funding from European Union's Horizon 2020 Research and Innovation Programme (Grant Agreement No. 802615).

REFERENCES

- ¹M. A. Zidan, J. P. Strachan, and W. D. Lu, *Nat. Electron.* **1**(1), 22–29 (2018).
- ²K. Duygu, Y. Shimeng, and H. S. P. Wong, *Nanotechnology* **24**(38), 382001 (2013).
- ³D. Ielmini and H. S. P. Wong, *Nat. Electron.* **1**(6), 333–343 (2018).
- ⁴C. D. James, J. B. Aimone, N. E. Miner, C. M. Vineyard, F. H. Rothganger, K. D. Carlson, S. A. Mulder, T. J. Draelos, A. Faust, M. J. Marinella, J. H. Naegle, and S. J. Plimpton, *Biol. Inspired Cognit. Archit.* **19**, 49–64 (2017).
- ⁵C. D. Harvey and K. Svoboda, *Nature* **450**, 1195 (2007).
- ⁶L. F. Abbott and S. B. Nelson, *Nat. Neurosci.* **3**(11), 1178–1183 (2000).
- ⁷L. F. Abbott and W. G. Regehr, *Nature* **431**(7010), 796–803 (2004).
- ⁸M. A. Lynch, *Physiol. Rev.* **84**(1), 87–136 (2004).
- ⁹D. Hebb, *The Organization of Behavior* (Wiley, New York, 1949).
- ¹⁰D. O. Hebb and D. Donderi, *Textbook of Psychology (Psychology Revivals)* (Psychology Press, 2013).
- ¹¹M. Bear, L. Cooper, and F. Ebner, *Science* **237**(4810), 42–48 (1987).
- ¹²N. Caporale and Y. Dan, *Annu. Rev. Neurosci.* **31**(1), 25–46 (2008).
- ¹³T. Masquelier, R. Guyonneau, and S. J. Thorpe, *Neural Comput.* **21**(5), 1259–1276 (2009).
- ¹⁴G. Rachmuth, H. Z. Shouval, M. F. Bear, and C.-S. Poon, *Proc. Natl. Acad. Sci.* **108**(49), E1266–E1274 (2011).
- ¹⁵C. Diorio, P. Hasler, A. Minch, and C. A. Mead, *IEEE Trans. Electron Devices* **43**(11), 1972–1980 (1996).
- ¹⁶P. E. Hasler, C. Diorio, B. A. Minch, and C. Mead, paper presented at the Advances in Neural Information Processing Systems, 1995.
- ¹⁷G. Indiveri, B. Linares-Barranco, T. Hamilton, A. van Schaik, R. Etienne-Cummings, T. Delbruck, S.-C. Liu, P. Dudek, P. Häfliger, S. Renaud, J. Schemmel, G. Cauwenberghs, J. Arthur, K. Hynna, F. Folowosele, S. Saighi, T. Serrano-Gotarredona, J. Wijekoon, Y. Wang, and K. Boahen, *Front. Neurosci.* **5**, 73 (2011).
- ¹⁸P. A. Merolla, J. V. Arthur, R. Alvarez-Icaza, A. S. Cassidy, J. Sawada, F. Akopyan, B. L. Jackson, N. Imam, C. Guo, Y. Nakamura, B. Brezzo, I. Vo, S. K. Esser, R. Appuswamy, B. Taba, A. Amir, M. D. Flickner, W. P. Risk, R. Manohar, and D. S. Modha, *Science* **345**(6197), 668–673 (2014).
- ¹⁹F. Akopyan, J. Sawada, A. Cassidy, R. Alvarez-Icaza, J. Arthur, P. Merolla, N. Imam, Y. Nakamura, P. Datta, G. Nam, B. Taba, M. Beakes, B. Brezzo, J. B. Kuang, R. Manohar, W. P. Risk, B. Jackson, and D. S. Modha, *IEEE Trans. Comput. Aided Des.* **34**(10), 1537–1557 (2015).
- ²⁰M. Davies, N. Srinivasa, T. Lin, G. Chinya, Y. Cao, S. H. Choday, G. Dimou, P. Joshi, N. Imam, S. Jain, Y. Liao, C. Lin, A. Lines, R. Liu, D. Mathaikutty, S. McCoy, A. Paul, J. Tse, G. Venkataraman, Y. Weng, A. Wild, Y. Yang, and H. Wang, *IEEE Micro* **38**(1), 82–99 (2018).
- ²¹Q. Xia and J. J. Yang, *Nat. Mater.* **18**(4), 309–323 (2019).
- ²²Y. van de Burgt, A. Melianas, S. T. Keene, G. Malliaras, and A. Salleo, *Nat. Electron.* **1**(7), 386–397 (2018).
- ²³Z. Y. Wang, L. Y. Wang, M. Nagai, L. H. Xie, M. D. Yi, and W. Huang, *Adv. Electron. Mater.* **3**(7), 1600510 (2017).
- ²⁴L. Chua, *IEEE Trans. Circuit Theory* **18**(5), 507–519 (1971).
- ²⁵L. O. Chua and K. S. Mo, *Proc. IEEE* **64**(2), 209–223 (1976).
- ²⁶D. B. Strukov, G. S. Snider, D. R. Stewart, and R. S. Williams, *Nature* **453**(7191), 80–83 (2008).
- ²⁷J. J. Yang, M. D. Pickett, X. Li, D. A. A. Ohlberg, D. R. Stewart, and R. S. Williams, *Nat. Nanotechnol.* **3**, 429 (2008).
- ²⁸J. G. Simmons, R. R. Verderber, and N. F. Mott, *Proc. R. Soc. London, Ser. A* **301**(1464), 77–102 (1967).
- ²⁹T. W. Hickmott, *J. Appl. Phys.* **33**(9), 2669–2682 (1962).
- ³⁰R. Waser and M. Aono, *Nat. Mater.* **6**(11), 833–840 (2007).
- ³¹S. P. Adhikari, M. P. Sah, H. Kim, and L. O. Chua, *IEEE Trans. Circuits Syst. I* **60**(11), 3008–3021 (2013).
- ³²I. Valov, E. Linn, S. Tappertzhofen, S. Schmelzer, J. van den Hurk, F. Lentz, and R. Waser, *Nat. Commun.* **4**(1), 1771 (2013).
- ³³T. Ohno, T. Hasegawa, T. Tsuruoka, K. Terabe, J. K. Gimzewski, and M. Aono, *Nat. Mater.* **10**(8), 591–595 (2011).
- ³⁴Z. Wang, S. Joshi, S. E. Savel'ev, H. Jiang, R. Midya, P. Lin, M. Hu, N. Ge, J. P. Strachan, Z. Li, Q. Wu, M. Barnell, G.-L. Li, H. L. Xin, R. S. Williams, Q. Xia, and J. J. Yang, *Nat. Mater.* **16**, 101 (2017).
- ³⁵Y. Yang, P. Gao, L. Li, X. Pan, S. Tappertzhofen, S. Choi, R. Waser, I. Valov, and W. D. Lu, *Nat. Commun.* **5**(1), 4232 (2014).
- ³⁶A. Sengupta and K. Roy, *Appl. Phys. Rev.* **4**(4), 041105 (2017).
- ³⁷X. Zhu, D. Li, X. Liang, and W. D. Lu, *Nat. Mater.* **18**(2), 141–148 (2019).
- ³⁸X. Sun, P. Wang, K. Ni, S. Datta, and S. Yu, paper presented at the 2018 IEEE International Electron Devices Meeting (IEDM), 2018.
- ³⁹B. C. Jiang, S. Kim, S. Y. Yang, J. Park, J.-H. Cha, J. Oh, J. Choi, S. G. Im, V. P. Dravid, and S.-Y. Choi, *Nano Lett.* **19**(2), 839–849 (2019).
- ⁴⁰G. Milano, S. Porro, I. Valov, and C. Ricciardi, *Adv. Electron. Mater.* **5**(9), 1800909 (2019).
- ⁴¹D. Kuzum, R. G. D. Jeyasingh, B. Lee, and H. S. P. Wong, *Nano Lett.* **12**(5), 2179–2186 (2012).
- ⁴²A. F. Vincent, J. Larroque, N. Locatelli, N. B. Romdhane, O. Bichler, C. Gramat, W. S. Zhao, J. Klein, S. Galdin-Retailleau, and D. Querlioz, *IEEE Trans. Biomed. Circuits Syst.* **9**(2), 166–174 (2015).
- ⁴³S. Boyn, J. Grollier, G. Lecerf, B. Xu, N. Locatelli, S. Fusil, S. Girod, C. Carrétéro, K. Garcia, S. Xavier, J. Tomas, L. Bellaiche, M. Bibes, A. Barthélémy, S. Saighi, and V. Garcia, *Nat. Commun.* **8**(1), 14736 (2017).
- ⁴⁴A. Wedig, M. Luebben, D.-Y. Cho, M. Moors, K. Skaja, V. Rana, T. Hasegawa, K. K. Adepalli, B. Yildiz, R. Waser, and I. Valov, *Nat. Nanotechnol.* **11**, 67 (2016).
- ⁴⁵H. F. Ling, K. M. Tan, Q. Y. Fang, X. S. Xu, H. Chen, W. W. Li, Y. F. Liu, L. Y. Wang, M. D. Yi, R. Huang, Y. Qian, L. H. Xie, and W. Huang, *Adv. Electron. Mater.* **3**(8), 1600416 (2017).
- ⁴⁶W. Zhongrui, R. Mingyi, M. Rivu, J. Saumil, J. Hao, L. Peng, S. Wenhao, A. Shiva, Z. Ye, L. Can, W. Huaqiang, X. Qiangfei, and Y. J. Joshua, *Adv. Funct. Mater.* **28**(6), 1704862 (2018).
- ⁴⁷I. Valov, I. Sapezanskaia, A. Nayak, T. Tsuruoka, T. Bredow, T. Hasegawa, G. Staikov, M. Aono, and R. Waser, *Nat. Mater.* **11**(6), 530–535 (2012).
- ⁴⁸H. Ling, M. Yi, M. Nagai, L. Xie, L. Wang, B. Hu, and W. Huang, *Adv. Mater.* **29**(35), 1701333 (2017).
- ⁴⁹T. Tsuruoka, K. Terabe, T. Hasegawa, I. Valov, R. Waser, and M. Aono, *Adv. Funct. Mater.* **22**(1), 70–77 (2012).
- ⁵⁰M. Lanza, H. S. P. Wong, E. Pop, D. Ielmini, D. Strukov, B. C. Regan, L. Larcher, M. A. Villena, J. J. Yang, L. Goux, A. Belmonte, Y. Yang, F. M. Puglisi, J. Kang, B. Magyari-Köpe, E. Yalon, A. Kenyon, M. Buckwell, A. Mehonic, A. Shluger, H. Li, T.-H. Hou, B. Hudec, D. Akinwande, R. Ge, S. Ambrogio, J. B. Roldan, E. Miranda, J. Suñe, K. L. Pey, X. Wu, N. Raghavan, E. Wu, W. D. Lu, G. Navarro, W. Zhang, H. Wu, R. Li, A. Holleitner, U. Wurstbauer, M. C. Lemme, M. Liu, S. Long, Q. Liu, H. Lv, A. Padovani, P. Pavan, I. Valov, X. Jing, T. Han, K. Zhu, S. Chen, F. Hui, and Y. Shi, *Adv. Electron. Mater.* **5**(1), 1800143 (2019).

- ⁵¹Z. Wang, C. Li, W. Song, M. Rao, D. Belkin, Y. Li, P. Yan, H. Jiang, P. Lin, M. Hu, J. P. Strachan, N. Ge, M. Barnell, Q. Wu, A. G. Barto, Q. Qiu, R. S. Williams, Q. Xia, and J. J. Yang, *Nat. Electron.* **2**(3), 115–124 (2019).
- ⁵²P. M. Sheridan, F. Cai, C. Du, W. Ma, Z. Zhang, and W. D. Lu, *Nat. Nanotechnol.* **12**, 784 (2017).
- ⁵³Z. Wang, S. Joshi, S. Savel'ev, W. Song, R. Midya, Y. Li, M. Rao, P. Yan, S. Asapu, Y. Zhuo, H. Jiang, P. Lin, C. Li, J. H. Yoon, N. K. Upadhyay, J. Zhang, M. Hu, J. P. Strachan, M. Barnell, Q. Wu, H. Wu, R. S. Williams, Q. Xia, and J. J. Yang, *Nat. Electron.* **1**(2), 137–145 (2018).
- ⁵⁴Y. Yu, Q. Ma, H. Ling, W. Li, R. Ju, L. Bian, N. Shi, Y. Qian, M. Yi, L. Xie, and W. Huang, *Adv. Funct. Mater.* **29**, 1904602 (2019).
- ⁵⁵S. Dai, Y. Zhao, Y. Wang, J. Zhang, L. Fang, S. Jin, Y. Shao, and J. Huang, *Adv. Funct. Mater.* **29**, 1903700 (2019).
- ⁵⁶H. Han, H. Yu, H. Wei, J. Gong, and W. Xu, *Small* **15**(32), 1900695 (2019).
- ⁵⁷C. D. Danesh, C. M. Shaffer, D. Nathan, R. Shenoy, A. Tudor, M. Tadayon, Y. Lin, and Y. Chen, *Adv. Mater.* **31**, 1808032 (2019).
- ⁵⁸Y. van de Burgt, E. Lubberman, E. J. Fuller, S. T. Keene, G. C. Faria, S. Agarwal, M. J. Marinella, A. Alec Talin, and A. Salleo, *Nat. Mater.* **16**, 414 (2017).
- ⁵⁹J. R. Abraham, L. Fucai, C. N. Anh, K. M. R. Z. Chao, F. Qundong, B. Arindam, L. Zheng, and M. Nripan, *Adv. Mater.* **30**(25), 1800220 (2018).
- ⁶⁰J. Y. Gerasimov, R. Gabriellson, R. Forchheimer, E. Stavrinidou, D. T. Simon, M. Berggren, and S. Fabiano, *Adv. Sci.* **6**(7), 1801339 (2019).
- ⁶¹J.-T. Yang, C. Ge, J.-Y. Du, H.-Y. Huang, M. He, C. Wang, H.-B. Lu, G.-Z. Yang, and K.-J. Jin, *Adv. Mater.* **30**(34), 1801548 (2018).
- ⁶²Z. Zhang, T. Li, Y. Wu, Y. Jia, C. Tan, X. Xu, G. Wang, J. Lv, W. Zhang, Y. He, J. Pei, C. Ma, G. Li, H. Xu, L. Shi, H. Peng, and H. Li, *Adv. Mater.* **31**(3), 1805769 (2019).
- ⁶³Z. Song, Y. Tong, X. Zhao, H. Ren, Q. Tang, and Y. Liu, *Mater. Horiz.* **6**(4), 717–726 (2019).
- ⁶⁴D.-G. Seo, Y. Lee, G.-T. Go, M. Pei, S. Jung, Y. H. Jeong, W. Lee, H.-L. Park, S.-W. Kim, H. Yang, C. Yang, and T.-W. Lee, *Nano Energy* **65**, 104035 (2019).
- ⁶⁵N. Liu, Y. Liu, J. Hu, Y. He, X. Zhang, and Q. Wan, *Appl. Surf. Sci.* **481**, 1412–1417 (2019).
- ⁶⁶M. Giordani, M. Berto, M. Di Lauro, C. A. Bortolotti, M. Zoli, and F. Biscarini, *ACS Sens.* **2**(12), 1756–1760 (2017).
- ⁶⁷E. R. W. van Doremalee, P. Gkoupidenis, and Y. van de Burgt, *J. Mater. Chem. C* **7**, 12754–12760 (2019).
- ⁶⁸Y. Lee and T.-W. Lee, *Acc. Chem. Res.* **52**(4), 964–974 (2019).
- ⁶⁹J. Li, W. Tang, Q. Wang, W. Sun, Q. Zhang, X. Guo, X. Wang, and F. Yan, *Mater. Sci. Eng., R* **127**, 1–36 (2018).
- ⁷⁰P. Lin and F. Yan, *Adv. Mater.* **24**(1), 34–51 (2012).
- ⁷¹N. Wang, A. Yang, Y. Fu, Y. Li, and F. Yan, *Acc. Chem. Res.* **52**(2), 277–287 (2019).
- ⁷²S. M. Won, E. Song, J. Zhao, J. Li, J. Rivnay, and J. A. Rogers, *Adv. Mater.* **30**(30), 1800534 (2018).
- ⁷³J. Rivnay, S. Inal, A. Salleo, R. M. Owens, M. Berggren, and G. G. Malliaras, *Nat. Rev. Mater.* **3**, 17086 (2018).
- ⁷⁴E. J. Fuller, S. T. Keene, A. Melianas, Z. Wang, S. Agarwal, Y. Li, Y. Tuchman, C. D. James, M. J. Marinella, J. J. Yang, A. Salleo, and A. A. Talin, *Science* **364**(6440), 570–574 (2019).
- ⁷⁵E. Juzekava, A. Nasretidinov, S. Battistoni, T. Berzina, S. Iannotta, R. Khazipov, V. Erokhin, and M. Mukhtarov, *Adv. Mater. Technol.* **4**(1), 1800350 (2019).
- ⁷⁶P. Gkoupidenis, D. A. Koutsouras, and G. G. Malliaras, *Nat. Commun.* **8**, 15448 (2017).
- ⁷⁷P. Gkoupidenis, D. A. Koutsouras, T. Lonjaret, J. A. Fairfield, and G. G. Malliaras, *Sci. Rep.* **6**, 27007 (2016).
- ⁷⁸S. Jia, F. Ying, and W. Qing, *J. Phys. D: Appl. Phys.* **51**(31), 314004 (2018).
- ⁷⁹P. Greengard, *Science* **294**(5544), 1024–1030 (2001).
- ⁸⁰A. E. Pereda, *Nat. Rev. Neurosci.* **15**, 250 (2014).
- ⁸¹W. H. Brattain and C. G. B. Garrett, *Bell Syst. Tech. J.* **34**(1), 129–176 (1955).
- ⁸²S. H. Kim, K. Hong, W. Xie, K. H. Lee, S. Zhang, T. P. Lodge, and C. D. Frisbie, *Adv. Mater.* **25**(13), 1822–1846 (2013).
- ⁸³Y. He, Y. Yang, S. Nie, R. Liu, and Q. Wan, *J. Mater. Chem. C* **6**(20), 5336–5352 (2018).
- ⁸⁴C. R. Newman, C. D. Frisbie, D. A. da Silva Filho, J.-L. Brédas, P. C. Ewbank, and K. R. Mann, *Chem. Mater.* **16**(23), 4436–4451 (2004).
- ⁸⁵D. Tu, L. Kergoat, X. Crispin, M. Berggren, and R. Forchheimer, “Transient analysis of electrolyte-gated organic field-effect transistors,” *Proc. SPIE* **8478**, 84780L (2012).
- ⁸⁶J. Rivnay, P. Leleux, M. Ferro, M. Sessolo, A. Williamson, D. A. Koutsouras, D. Khodagholy, M. Ramuz, X. Strakosas, R. M. Owens, C. Benar, J.-M. Badier, C. Bernard, and G. G. Malliaras, *Sci. Adv.* **1**(4), e1400251 (2015).
- ⁸⁷M. Moser, J. F. Ponder, Jr., A. Wadsworth, A. Giovannitti, and I. McCulloch, *Adv. Funct. Mater.* **29**(21), 1807033 (2019).
- ⁸⁸D. A. Bernards and G. G. Malliaras, *Adv. Funct. Mater.* **17**(17), 3538–3544 (2007).
- ⁸⁹J. Zhou, Y. Liu, Y. Shi, and Q. Wan, *IEEE Electron Device Lett.* **35**(2), 280–282 (2014).
- ⁹⁰L. Q. Zhu, C. J. Wan, L. Q. Guo, Y. Shi, and Q. Wan, *Nat. Commun.* **5**, 3158 (2014).
- ⁹¹H. K. Li, T. P. Chen, P. Liu, S. G. Hu, Y. Liu, Q. Zhang, and P. S. Lee, *J. Appl. Phys.* **119**(24), 244505 (2016).
- ⁹²J. Sun, S. Oh, Y. Choi, S. Seo, M. J. Oh, M. Lee, W. B. Lee, P. J. Yoo, J. H. Cho, and J. H. Park, *Adv. Funct. Mater.* **28**(47), 1804397 (2018).
- ⁹³Q. Wu, J. Wang, J. Cao, C. Lu, G. Yang, X. Shi, X. Chuai, Y. Gong, Y. Su, Y. Zhao, N. Lu, D. Geng, H. Wang, L. Li, and M. Liu, *Adv. Electron. Mater.* **4**(12), 1800556 (2018).
- ⁹⁴M. Lee, W. Lee, S. Choi, J. W. Jo, J. Kim, S. K. Park, and Y. H. Kim, *Adv. Mater.* **29**(28), 1700951 (2017).
- ⁹⁵R. A. John, J. Ko, M. R. Kulkarni, N. Tiwari, N. A. Chien, N. G. Ing, W. L. Leong, and N. Mathews, *Small* **13**(32), 1701193 (2017).
- ⁹⁶H. Tian, W. Mi, X.-F. Wang, H. Zhao, Q.-Y. Xie, C. Li, Y.-X. Li, Y. Yang, and T.-L. Ren, *Nano Lett.* **15**(12), 8013–8019 (2015).
- ⁹⁷M. T. Sharbati, Y. Du, J. Torres, N. D. Ardolino, M. Yun, and F. Xiong, *Adv. Mater.* **30**(36), 1802353 (2018).
- ⁹⁸Y. Yao, X. Huang, S. Peng, D. Zhang, J. Shi, G. Yu, Q. Liu, and Z. Jin, *Adv. Electron. Mater.* **5**(5), 1800887 (2019).
- ⁹⁹J. Jie, G. Junjie, W. Xiang, Y. Yi, X. Haipeng, N. Dongmei, Y. Junliang, H. Jun, G. Yongli, and W. Qing, *Small* **13**(29), 1700933 (2017).
- ¹⁰⁰D. Xie, J. Jiang, W. Hu, Y. He, J. Yang, J. He, Y. Gao, and Q. Wan, *ACS Appl. Mater. Interfaces* **10**(31), 25943–25948 (2018).
- ¹⁰¹C.-S. Yang, D.-S. Shang, N. Liu, E. J. Fuller, S. Agrawal, A. A. Talin, Y.-Q. Li, B.-G. Shen, and Y. Sun, *Adv. Funct. Mater.* **28**(42), 1804170 (2018).
- ¹⁰²C. S. Yang, D. S. Shang, N. Liu, G. Shi, X. Shen, R. C. Yu, Y. Q. Li, and Y. Sun, *Adv. Mater.* **29**(27), 1700906 (2017).
- ¹⁰³J. Zhu, Y. Yang, R. Jia, Z. Liang, W. Zhu, Z. U. Rehman, L. Bao, X. Zhang, Y. Cai, L. Song, and R. Huang, *Adv. Mater.* **30**(21), 1800195 (2018).
- ¹⁰⁴S. Kim, J. Yoon, H.-D. Kim, and S.-J. Choi, *ACS Appl. Mater. Interfaces* **7**(45), 25479–25486 (2015).
- ¹⁰⁵K. Kim, C. L. Chen, Q. Truong, A. M. Shen, and Y. Chen, *Adv. Mater.* **25**(12), 1693–1698 (2013).
- ¹⁰⁶D. Sarkar, J. Tao, W. Wang, Q. Lin, M. Yeung, C. Ren, and R. Kapadia, *ACS Nano* **12**(2), 1656–1663 (2018).
- ¹⁰⁷Y. Lee, J. Y. Oh, W. Xu, O. Kim, T. R. Kim, J. Kang, Y. Kim, D. Son, J. B.-H. Tok, M. J. Park, Z. Bao, and T.-W. Lee, *Sci. Adv.* **4**(11), eaat7387 (2018).
- ¹⁰⁸W. Xu, S. Y. Min, H. Hwang, and T. W. Lee, *Sci. Adv.* **2**(6), e1501326 (2016).
- ¹⁰⁹P. Gkoupidenis, N. Schaefer, B. Garlan, and G. G. Malliaras, *Adv. Mater.* **27**(44), 7176–7180 (2015).
- ¹¹⁰C. Qian, J. Sun, L.-a. Kong, G. Gou, J. Yang, J. He, Y. Gao, and Q. Wan, *ACS Appl. Mater. Interfaces* **8**(39), 26169–26175 (2016).
- ¹¹¹C. Qian, L.-A. Kong, J. Yang, Y. Gao, and J. Sun, *Appl. Phys. Lett.* **110**(8), 083302 (2017).
- ¹¹²D. A. Lapkin, A. V. Emelyanov, V. A. Demin, T. S. Berzina, and V. V. Erokhin, *Microelectron. Eng.* **185–186**, 43–47 (2018).
- ¹¹³S. Battistoni, V. Erokhin, and S. Iannotta, *Org. Electron.* **65**, 434–438 (2019).
- ¹¹⁴S. Dai, Y. Wang, J. Zhang, Y. Zhao, F. Xiao, D. Liu, T. Wang, and J. Huang, *ACS Appl. Mater. Interfaces* **10**(46), 39983–39991 (2018).
- ¹¹⁵S. Desbief, M. di Lauro, S. Casalini, D. Guerin, S. Tortorella, M. Barbalinardo, A. Kyndiah, M. Murgia, T. Cramer, F. Biscarini, and D. Vuillaume, *Org. Electron.* **38**, 21–28 (2016).
- ¹¹⁶Y. H. Liu, L. Qiang Zhu, Y. Shi, and Q. Wan, *Appl. Phys. Lett.* **104**(13), 133504 (2014).

- ¹¹⁷X. Fan, B. Xu, N. Wang, J. Wang, S. Liu, H. Wang, and F. Yan, *Adv. Electron. Mater.* **3**(5), 1600471 (2017).
- ¹¹⁸R. S. Zucker and W. G. Regehr, *Annu. Rev. Physiol.* **64**(1), 355–405 (2002).
- ¹¹⁹E. S. Fortune and G. J. Rose, *J. Neurosci.* **20**(18), 7122–7130 (2000).
- ¹²⁰B. James, L. Darnet, J. Moya-Díaz, S.-H. Seibel, and L. Lagnado, *Nat. Neurosci.* **22**(7), 1140–1147 (2019).
- ¹²¹J. A. Kauer and R. C. Malenka, *Nat. Rev. Neurosci.* **8**, 844 (2007).
- ¹²²R. A. Nicoll, *Neuron* **93**(2), 281–290 (2017).
- ¹²³Q. Lai, L. Zhang, Z. Li, W. F. Stickle, R. S. Williams, and Y. Chen, *Adv. Mater.* **22**(22), 2448–2453 (2010).
- ¹²⁴C. L. Chen, K. Kim, Q. Truong, A. Shen, Z. Li, and Y. Chen, *Nanotechnology* **23**(27), 275202 (2012).
- ¹²⁵J. Zhou, N. Liu, L. Zhu, Y. Shi, and Q. Wan, *IEEE Electron Device Lett.* **36**(2), 198–200 (2015).
- ¹²⁶H. Ling, N. Wang, A. Yang, Y. Liu, J. Song, and F. Yan, *Adv. Mater. Technol.* **4**(9), 1900471 (2019).
- ¹²⁷L.-A. Kong, J. Sun, C. Qian, C. Wang, J. Yang, and Y. Gao, *Org. Electron.* **44**, 25–31 (2017).
- ¹²⁸T. V. P. Bliss, G. L. Collingridge, R. G. M. Morris, and G. M. Morris Richard, *Philosoph. Trans. R. Soc. London, Ser. B* **358**(1432), 643–647 (2003).
- ¹²⁹R. C. Malenka and M. F. Bear, *Neuron* **44**(1), 5–21 (2004).
- ¹³⁰S. T. Keene, A. Melianas, Y. v d Burgt, and A. Salleo, *Adv. Electron. Mater.* **5**(2), 1800686 (2019).
- ¹³¹S. T. Keene, A. Melianas, E. J. Fuller, Y. V. D. Burgt, A. A. Talin, and A. Salleo, *J. Phys. D: Appl. Phys.* **51**(22), 224002 (2018).
- ¹³²P. Gkoupidenis, N. Schaefer, X. Strakosas, J. A. Fairfield, and G. G. Malliaras, *Appl. Phys. Lett.* **107**(26), 263302 (2015).
- ¹³³B. Winther-Jensen, B. Kolodziejczyk, and O. Winther-Jensen, *APL Mater.* **3**(1), 014903 (2015).
- ¹³⁴L. A. Kong, J. Sun, C. Qian, Y. Fu, J. X. Wang, J. L. Yang, and Y. L. Gao, *Org. Electron.* **47**, 126–132 (2017).
- ¹³⁵D. Lee, J. Park, K. Moon, J. Jang, S. Park, M. Chu, J. Kim, J. Noh, M. Jeon, B. H. Lee, B. Lee, B. Lee, and H. Hwang, paper presented at the 2015 IEEE International Electron Devices Meeting (IEDM), 2015.
- ¹³⁶H. Wang, Q. Zhao, Z. Ni, Q. Li, H. Liu, Y. Yang, L. Wang, Y. Ran, Y. Guo, W. Hu, and Y. Liu, *Adv. Mater.* **30**(46), 1803961 (2018).
- ¹³⁷E. J. Fuller, F. E. Gabaly, F. Leonard, S. Agarwal, S. J. Plimpton, R. B. Jacobs-Gedrim, C. D. James, M. J. Marinella, and A. A. Talin, *Adv. Mater.* **29**(4), 1604310 (2017).
- ¹³⁸G. G. Turrigiano and S. B. Nelson, *Curr. Opin. Neurobiol.* **10**(3), 358–364 (2000).
- ¹³⁹G. G. Turrigiano and S. B. Nelson, *Nat. Rev. Neurosci.* **5**(2), 97–107 (2004).
- ¹⁴⁰D. A. Koutsouras, G. G. Malliaras, and P. Gkoupidenis, *MRS Commun.* **8**(2), 493–497 (2018).
- ¹⁴¹D. A. Koutsouras, T. Prodromakis, G. G. Malliaras, P. W. M. Blom, and P. Gkoupidenis, *Adv. Intell. Syst.* **1**(1), 1900013 (2019).
- ¹⁴²H. F. Ling, S. H. Liu, Z. J. Zheng, and F. Yan, *Small Methods* **2**(10), 1800070 (2018).
- ¹⁴³S.-W. Hwang, H. Tao, D.-H. Kim, H. Cheng, J.-K. Song, E. Rill, M. A. Brenckle, B. Panilaitis, S. M. Won, Y.-S. Kim, Y. M. Song, K. J. Yu, A. Ameen, R. Li, Y. Su, M. Yang, D. L. Kaplan, M. R. Zakin, M. J. Slepian, Y. Huang, F. G. Omenetto, and J. A. Rogers, *Science* **337**(6102), 1640–1644 (2012).
- ¹⁴⁴S. Inal, J. Rivnay, A.-O. Sui, G. G. Malliaras, and I. McCulloch, *Acc. Chem. Res.* **51**(6), 1368–1376 (2018).
- ¹⁴⁵Y. Anneng, L. Yuanzhe, Y. Chenxiao, F. Ying, W. Naixiang, L. Li, and Y. Feng, *Adv. Mater.* **30**(23), 1800051 (2018).
- ¹⁴⁶J. Rivnay, P. Leleux, M. Sessolo, D. Khodagholy, T. Hervé, M. Fiocchi, and G. G. Malliaras, *Adv. Mater.* **25**(48), 7010–7014 (2013).
- ¹⁴⁷S. Inal, G. G. Malliaras, and J. Rivnay, *Nat. Commun.* **8**(1), 1767 (2017).
- ¹⁴⁸A. Laiho, L. Herlogsson, R. Forchheimer, X. Crispin, and M. Berggren, *Proc. Natl. Acad. Sci.* **108**(37), 15069–15073 (2011).
- ¹⁴⁹A. Giovannitti, D.-T. Sbircea, S. Inal, C. B. Nielsen, E. Bandiello, D. A. Hanifi, M. Sessolo, G. G. Malliaras, I. McCulloch, and J. Rivnay, *Proc. Natl. Acad. Sci.* **113**(43), 12017–12022 (2016).
- ¹⁵⁰C. Cendra, A. Giovannitti, A. Savva, V. Venkatraman, I. McCulloch, A. Salleo, S. Inal, and J. Rivnay, *Adv. Funct. Mater.* **29**(5), 1807034 (2019).
- ¹⁵¹A. Giovannitti, C. B. Nielsen, D.-T. Sbircea, S. Inal, M. Donahue, M. R. Niazi, D. A. Hanifi, A. Amassian, G. G. Malliaras, J. Rivnay, and I. McCulloch, *Nat. Commun.* **7**, 13066 (2016).
- ¹⁵²A. M. Pappa, D. Ohayon, A. Giovannitti, I. P. Maria, A. Savva, I. Uguz, J. Rivnay, I. McCulloch, R. M. Owens, and S. Inal, *Sci. Adv.* **4**(6), eaat0911 (2018).
- ¹⁵³H. Sun, M. Vagin, S. Wang, X. Crispin, R. Forchheimer, M. Berggren, and S. Fabiano, *Adv. Mater.* **30**(9), 1704916 (2018).
- ¹⁵⁴B. C.-K. Tee, A. Chortos, A. Berndt, A. K. Nguyen, A. Tom, A. McGuire, Z. C. Lin, K. Tien, W.-G. Bae, H. Wang, P. Mei, H.-H. Chou, B. Cui, K. Deisseroth, T. N. Ng, and Z. Bao, *Science* **350**(6258), 313–316 (2015).
- ¹⁵⁵L. Shenghua, F. Ying, L. Guijun, L. Li, L. H. Ka-wai, C. Xianfeng, and Y. Feng, *Adv. Mater.* **29**(35), 1701733 (2017).
- ¹⁵⁶C. Ge, C. X. Liu, Q. L. Zhou, Q. H. Zhang, J. Y. Du, J. K. Li, C. Wang, L. Gu, G. Z. Yang, and K. J. Jin, *Adv. Mater.* **31**(19), 1900379 (2019).
- ¹⁵⁷K. H. Lee, M. S. Kang, S. Zhang, Y. Gu, T. P. Lodge, and C. D. Frisbie, *Adv. Mater.* **24**(32), 4457–4462 (2012).
- ¹⁵⁸S. K. Hwang, T. J. Park, K. L. Kim, S. M. Cho, B. J. Jeong, and C. Park, *ACS Appl. Mater. Interfaces* **6**(22), 20179–20187 (2014).
- ¹⁵⁹A.-M. Pappa, S. Inal, K. Roy, Y. Zhang, C. Pitsalidis, A. Hama, J. Pas, G. G. Malliaras, and R. M. Owens, *ACS Appl. Mater. Interfaces* **9**(12), 10427–10434 (2017).
- ¹⁶⁰C. Zou, J. Sun, G. Gou, L.-A. Kong, C. Qian, G. Dai, J. Yang, and G.-H. Guo, *Appl. Phys. A* **123**(9), 597 (2017).
- ¹⁶¹C. J. Wan, Y. H. Liu, L. Q. Zhu, P. Feng, Y. Shi, and Q. Wan, *ACS Appl. Mater. Interfaces* **8**(15), 9762–9768 (2016).
- ¹⁶²F. Yu, L. Q. Zhu, W. T. Gao, Y. M. Fu, H. Xiao, J. Tao, and J. M. Zhou, *ACS Appl. Mater. Interfaces* **10**, 16881–16886 (2018).
- ¹⁶³S. D. Yambem, J. Timm, M. Weiss, A. K. Pandey, and R. Marschall, *Adv. Electron. Mater.* **3**(12), 1700316 (2017).
- ¹⁶⁴Y. H. Liu, L. Q. Zhu, P. Feng, Y. Shi, and Q. Wan, *Adv. Mater.* **27**(37), 5599–5604 (2015).
- ¹⁶⁵G. Wu, J. Zhang, X. Wan, Y. Yang, and S. Jiang, *J. Mater. Chem. C* **2**(31), 6249–6255 (2014).
- ¹⁶⁶A. Cifarelli, A. Parisini, T. Berzina, and S. Iannotta, *Microelectron. Eng.* **193**, 65–70 (2018).
- ¹⁶⁷F. Yu, L. Q. Zhu, H. Xiao, W. T. Gao, and Y. B. Guo, *Adv. Funct. Mater.* **28**(44), 1804025 (2018).
- ¹⁶⁸Y. Liu, X. Wan, L. Q. Zhu, Y. Shi, and Q. Wan, *IEEE Electron Device Lett.* **35**(12), 1257–1259 (2014).
- ¹⁶⁹A. Cifarelli, A. Parisini, S. Iannotta, and T. Berzina, *Microelectron. Eng.* **185–186**, 55–60 (2018).
- ¹⁷⁰L. Q. Guo, J. Tao, L. Q. Zhu, H. Xiao, W. T. Gao, F. Yu, and Y. M. Fu, *Org. Electron.* **61**, 312–317 (2018).
- ¹⁷¹G. Wu, P. Feng, X. Wan, L. Zhu, Y. Shi, and Q. Wan, *Sci. Rep.* **6**, 23578 (2016).
- ¹⁷²J. Zhang, J. Dai, L. Zhu, C. Chen, and Q. Wan, *IEEE Electron Device Lett.* **35**(8), 838–840 (2014).
- ¹⁷³X. Wan, P. Feng, G. D. Wu, Y. Shi, and Q. Wan, *IEEE Electron Device Lett.* **36**(2), 204–206 (2015).
- ¹⁷⁴G. J. Stuart and N. Spruston, *Nat. Neurosci.* **18**, 1713 (2015).
- ¹⁷⁵N. Spruston, *Nat. Rev. Neurosci.* **9**, 206 (2008).
- ¹⁷⁶P. Gkoupidenis, S. Rezaei-Mazinani, C. M. Proctor, E. Ismailova, and G. G. Malliaras, *AIP Adv.* **6**(11), 111307 (2016).
- ¹⁷⁷C. J. Wan, Y. H. Liu, P. Feng, W. Wang, L. Q. Zhu, Z. P. Liu, Y. Shi, and Q. Wan, *Adv. Mater.* **28**(28), 5878–5885 (2016).
- ¹⁷⁸Y. He, S. Nie, R. Liu, S. Jiang, Y. Shi, and Q. Wan, *Adv. Mater.* **31**(21), 1900903 (2019).
- ¹⁷⁹C. J. Wan, L. Q. Zhu, Y. H. Liu, P. Feng, Z. P. Liu, H. L. Cao, P. Xiao, Y. Shi, and Q. Wan, *Adv. Mater.* **28**(18), 3557–3563 (2016).
- ¹⁸⁰Y. Fu, L.-A. Kong, Y. Chen, J. Wang, C. Qian, Y. Yuan, J. Sun, Y. Gao, and Q. Wan, *ACS Appl. Mater. Interfaces* **10**(31), 26443–26450 (2018).
- ¹⁸¹R. Shapley, M. Hawken, and D. L. Ringach, *Neuron* **38**(5), 689–699 (2003).
- ¹⁸²N. J. Priebe and D. Ferster, *Neuron* **75**(2), 194–208 (2012).
- ¹⁸³J. S. Nettleton and W. J. Spain, *J. Neurophysiol.* **83**(6), 3310–3322 (2000).
- ¹⁸⁴A. Polsky, B. W. Mel, and J. Schiller, *Nat. Neurosci.* **7**(6), 621–627 (2004).
- ¹⁸⁵Y. Chen, W. Qiu, X. Wang, W. Liu, J. Wang, G. Dai, Y. Yuan, Y. Gao, and J. Sun, *Nano Energy* **62**, 393–400 (2019).

- ¹⁸⁶Y. Yang, Y. L. He, S. Nie, Y. Shi, and Q. Wan, *IEEE Electron Device Lett.* **39**(6), 897–900 (2018).
- ¹⁸⁷M. Chistiakova, N. M. Bannon, M. Bazhenov, and M. Volgushev, *Neuroscientist* **20**(5), 483–498 (2014).
- ¹⁸⁸N. Frémaux and W. Gerstner, *Front. Neural Circuits* **9**, 85 (2016).
- ¹⁸⁹R. A. John, N. Tiwari, C. Yaoyi, Ankit, N. Tiwari, M. Kulkarni, A. Nirmal, A. C. Nguyen, A. Basu, and N. Mathews, *ACS Nano* **12**(11), 11263–11273 (2018).
- ¹⁹⁰G. Daniel, *Principles of Artificial Neural Networks* (World Scientific, 2013).
- ¹⁹¹B. Widrow and M. A. Lehr, *Proc. IEEE* **78**(9), 1415–1442 (1990).
- ¹⁹²I. A. Basheer and M. Hajmeer, *J. Microbiol. Methods* **43**(1), 3–31 (2000).
- ¹⁹³D. E. Rumelhart, G. E. Hinton, and R. J. Williams, in *Cognitive Modeling*, edited by T. A. Polk and C. M. Seifert (MIT Press, 2002), Vol. 5, p. 1.
- ¹⁹⁴R. J. Erb, *Pharm. Res.* **10**(2), 165–170 (1993).
- ¹⁹⁵Y. Xin, *Proc. IEEE* **87**(9), 1423–1447 (1999).
- ¹⁹⁶S. Battistoni, V. Erokhin, and S. Iannotta, *J. Phys. D: Appl. Phys.* **51**(28), 284002 (2018).
- ¹⁹⁷A. V. Emelyanov, D. A. Lapkin, V. A. Demin, V. V. Erokhin, S. Battistoni, G. Baldi, A. Dimonte, A. N. Korovin, S. Iannotta, P. K. Kashkarov, and M. V. Kovalchuk, *AIP Adv.* **6**(11), 111301 (2016).
- ¹⁹⁸D. Khodagholy, J. Rivnay, M. Sessolo, M. Gurfinkel, P. Leleux, L. H. Jimison, E. Stavrinidou, T. Herve, S. Sanaur, R. M. Owens, and G. G. Malliaras, *Nat. Commun.* **4**, 2133 (2013).
- ¹⁹⁹N. Wang, Y. Liu, Y. Fu, and F. Yan, *ACS Appl. Mater. Interfaces* **10**(31), 25834–25840 (2018).
- ²⁰⁰C. Wan, G. Chen, Y. Fu, M. Wang, N. Matsuhisa, S. Pan, L. Pan, H. Yang, Q. Wan, L. Zhu, and X. Chen, *Adv. Mater.* **30**(30), 1801291 (2018).
- ²⁰¹E. Stavrinidou, R. Gabrielsson, E. Gomez, X. Crispin, O. Nilsson, D. T. Simon, and M. Berggren, *Sci. Adv.* **1**(10), e1501136 (2015).
- ²⁰²T. Cramer, B. Chelli, M. Murgia, M. Barbalinardo, E. Bystrenova, D. M. de Leeuw, and F. Biscarini, *Phys. Chem. Chem. Phys.* **15**(11), 3897–3905 (2013).
- ²⁰³G. Tarabella, P. D'Angelo, A. Cifarelli, A. Dimonte, A. Romeo, T. Berzina, V. Erokhin, and S. Iannotta, *Chem. Sci.* **6**(5), 2859–2868 (2015).
- ²⁰⁴A. Romeo, A. Dimonte, G. Tarabella, P. D'Angelo, V. Erokhin, and S. Iannotta, *APL Mater.* **3**(1), 014909 (2015).
- ²⁰⁵Y. Zang, H. Shen, D. Huang, C. A. Di, and D. Zhu, *Adv. Mater.* **29**(18), 1606088 (2017).
- ²⁰⁶Y. Kim, A. Chortos, W. Xu, Y. Liu, J. Y. Oh, D. Son, J. Kang, A. M. Foudeh, C. Zhu, Y. Lee, S. Niu, J. Liu, R. Pfattner, Z. Bao, and T.-W. Lee, *Science* **360**(6392), 998–1003 (2018).
- ²⁰⁷Y. Liu, J. Zhong, E. Li, H. Yang, X. Wang, D. Lai, H. Chen, and T. Guo, *Nano Energy* **60**, 377–384 (2019).
- ²⁰⁸S. Wang, C. Chen, Z. Yu, Y. He, X. Chen, Q. Wan, Y. Shi, D. W. Zhang, H. Zhou, X. Wang, and P. Zhou, *Adv. Mater.* **31**(3), 1806227 (2019).
- ²⁰⁹Y. Wang, Z. Lv, J. Chen, Z. Wang, Y. Zhou, L. Zhou, X. Chen, and S.-T. Han, *Adv. Mater.* **30**(38), 1802883 (2018).
- ²¹⁰Q. Shuchao, W. Fengqiu, L. Yujie, W. Qing, W. Xinran, X. Yongbing, S. Yi, W. Xiaomu, and Z. Rong, *2D Mater.* **4**(3), 035022 (2017).
- ²¹¹S. Seo, S.-H. Jo, S. Kim, J. Shim, S. Oh, J.-H. Kim, K. Heo, J.-W. Choi, C. Choi, S. Oh, D. Kuzum, H. S. P. Wong, and J.-H. Park, *Nat. Commun.* **9**(1), 5106 (2018).
- ²¹²H. Tian, X. Wang, F. Wu, Y. Yang, and T. Ren, paper presented at the 2018 IEEE International Electron Devices Meeting (IEDM), 2018.
- ²¹³G. D. Spyropoulos, J. N. Gelinas, and D. Khodagholy, *Sci. Adv.* **5**(2), eaau7378 (2019).
- ²¹⁴J. J. Yang and Q. Xia, *Nat. Mater.* **16**, 396 (2017).